Geochronology and geochemistry of Mesoproterozoic granitoids in the Lhasa terrane, south Tibet: implications for the early evolution of the Lhasa terrane

Journal Item

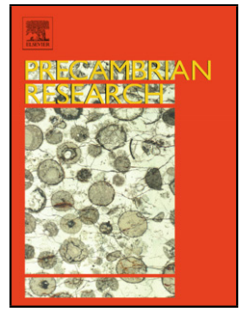

Title: Geochronology and geochemistry of Mesoproterozoic granitoids in the Lhasa terrane, south Tibet: Implications for the early evolution of Lhasa terrane

Author: Wang-Chun Xu Hong-Fei Zhang Nigel Harris Liang Guo Fa-Bin Pan Shuai Wang

PII:	S0301-9268(13)00227-1
DOI:	http://dx.doi.org/doi:10.1016/j.precamres.2013.07.016
Reference:	PRECAM 3815
To appear in:	*Precambrian Research*
Received date:	6-2-2013
Revised date:	15-7-2013
Accepted date:	19-7-2013

Please cite this article as: Xu, W.-C., Zhang, H.-F., Harris, N., Guo, L., Pan, F.-B., Wang, S., Geochronology and geochemistry of Mesoproterozoic granitoids in the Lhasa terrane, south Tibet: Implications for the early evolution of Lhasa terrane, *Precambrian Research* (2013), http://dx.doi.org/10.1016/j.precamres.2013.07.016

Geochronology and geochemistry of Mesoproterozoic granitoids in the Lhasa terrane, south Tibet: Implications for the early evolution of Lhasa terrane

Wang-Chun Xu[a*], Hong-Fei Zhang[a], Nigel Harris[b], Liang Guo[a], Fa-Bin Pan[a], Shuai Wang[a]

[a] *State Key Laboratory of Geological Processes and Mineral Resources, and Faculty of Earth Sciences, China University of Geosciences, Wuhan 430074, P.R. China*

[b] *Department of Environment, Earth and Ecosystems, The Open University, Milton Keynes, MK7 6AA,UK*

A revised manuscript submitting to Precambrian Research for review

* Corresponding author. e-mail: wcxu2003@163.com, phone number: +86 27 67883001, Fax: +86 27 67883002

Abstract

The early history of the Lhasa terrane remains poorly constrained due to the poor exposure of the Proterozoic rocks. We report here U-Pb zircon ages, geochemical and Hf isotopic data for granite gneisses and biotite gneisses from the Bomi Complex in the eastern part of the Lhasa terrane, south Tibet. Petrological and geochemical data suggest that the protoliths of the granite gneisses and the biotite gneisses could be granites and tonalites, respectively. LA-ICPMS U-Pb zircon analyses yielded ages of 1343±27 Ma (MSWD=0.3) and 1276±22 Ma (MSWD=0.4) for two granite gneisses, and a consistent age of ca. 1250 Ma for two biotite gneisses. These ages are interpreted as the magma crystallization time of both the gneisses protoliths, and thus the Bomi Complex represents the oldest rocks found in the Lhasa terrane. Our data indicate that the Mesoproterozoic detrital zircons from the Paleozoic metasedimentary rocks in the Lhasa terrane could be derived from the Lhasa terrane itself or the Tethyan Himalaya, rather than necessarily from the Albany-Fraser belt in the Australia. Geochemical characteristics show that the granite gneisses have an aluminous A-type granite affinity. The two granite gneisses dated in this study have zircon $\varepsilon_{Hf}(t)$ values between +4.0 and +1.8 and between +2.6 and +0.2, respectively. They have identical two-stage Hf model ages of ~2.0 Ga. We suggest that the protoliths of the granite gneisses were produced by protracted high temperature partial melting of a felsic intracrustal source in an extensional setting. In contrast, the biotite gneisses have similar geochemical characteristics to those of calc-alkaline granitoids that probably formed in a subduction-related environment. Zircons from the two dated biotite gneisses have relatively higher $\varepsilon_{Hf}(t)$ values of +8.1 to +3.6 and +10.5 to +5.7, respectively, indicating a juvenile mantle contribution to their magma source. Earlier magmatism at ~1343-1276 Ma may formed in a continental rift setting related to the final breakup of supercontinent Columbia, while subsequent magmatism of ~1250 Ma resulted from subduction of ocean slab during the assemblage

of Rodinia. We thus infer that the Bomi Complex was related to the contact zone between the Eastern Ghats Belt and the Archaean cratons in southeastern India during the Mesoproterozoic.

Keywords: Mesoproterozoic; tectonic evolution; aluminous A-type granite; Bomi Complex; Lhasa terrane

1. Introduction

It is widely assumed that the high elevation and thick crust of Tibet is largely a consequence of the Cenozoic collision and continued convergence between the Indian and Eurasian plates (Beck et al., 1995; de Sigoyer et al., 2000; Leech et al., 2005; Yin, 2006). The Lhasa terrane, the southern margin of the Eurasian continent, has received much attention as it records the history of both the pre-collision and the collision-related tectonism, magmatism and metamorphism (Zhu et al., 2011a; Zhang et al., 2012a). The Lhasa terrane is dominantly composed of Meso-Cenozoic igneous rocks and Paleozoic to Mesozoic sedimentary rocks with rare inliers of Precambrian basements (Yin and Harrison, 2000). Numerous studies of the Lhasa terrane that have been carried out over recent decades have focused largely on the Meso-Cenozoic igneous rocks, which have helped to develop an understanding of the Andean-type arc, India-Eurasian collision and related Cenozoic tectonic processes (Chung et al., 2005; Zhu et al., 2011b; and references therein). Although some of the previous studies referred to the Precambrian evolution (Dong et al., 2011; Guynn et al., 2011; Zhang et al., 2012a), the origin of the Lhasa terrane has remained enigmatic.

Understanding the origin of southern exposed edge of the Eurasian plate is crucial for unraveling the deformation history attending collision of Eurasia with India, and hence for reconstructing the position of the Lhasa terrane in the supercontinental assembly. Recently, Zhu et al. (2011a) published a set of U-Pb age and Hf isotope data on detrital zircons from Paleozoic metasedimentary rocks in the Lhasa terrane. These data define a distinctive age population of ca.1170 Ma with ε_{Hf}(t) values similar to coeval detrital zircons from Western Australia. In the absence of any recognised Mesoproterozoic rocks from the Lhasa terrane itself, the ca.1170 Ma detrital zircons were presumed to have been derived from the Albany-Fraser belt in southwest Australia (Zhu et al., 2011a). In the Paleozoic reconstruction, therefore, the Lhasa terrane was positioned at the northwestern margin of Australia proximal to Mesoproterozoic source regions. Thus the presence of Mesoproterozoic rocks in the Lhasa terrane has crucial implications for the geochemical and tectonic evolution of this block.

In the eastern Himalayan syntaxis, high-grade metamorphic rocks (Bomi Complex) are well exposed from rapid uplift and erosion (Burg et al., 1997). The Bomi Complex consists of orthogneisses, paragneisses, migmatites, and amphibolites. In this study, we carried out an integrated study of zircon U-Pb age, major and trace element geochemistry, and Lu-Hf isotope composition for the granite gneisses and biotite gneisses from the Bomi Complex. Our data show three episodes of Mesoproterozoic magmatism that may formed from a rift-related tectonic setting and a subduction-related process, respectively. The results can provide important insights into understanding the Mesoproterozoic tectonic evolution of the Lhasa terrane.

2. **Geological setting and sample description**

2.1. Regional geology

The eastern Himalayan syntaxis (EHS) is the eastern termination of the Himalaya collisional orogen (Fig.1). The EHS comprises three major tectono-stratigraphic units (Geng et al., 2006): (1) the Namche Barwa Complex of the Himalayan unit; (2) the Indus-Yarlung unit (IYS); and (3) the

Lhasa unit. The northwestern and southeastern contacts between the Namche Barwa Complex and the Lhasa unit are marked by the sinistral Dongjiu-Miling fault and dextral Aniqiao fault, respectively. The syntaxis is cut at its northeastern tip by the active dextral Jiali-Parlung fault (Burg et al., 1997; Burg et al., 1998; Zhang et al., 2004).

The Namche Barwa Complex, the core of the EHS, includes layered quartz-feldspar-biotite gneisses that are locally migmatised (Burg et al., 1998). According to recent geological mapping (Geng et al., 2006), the Namche Barwa Complex can be subdivided into three subunits: Zhibai Formation, Duoxiongla Complex and Paixiang Formation (Fig. 1), separated by ductile faults (Xu et al., 2008). The Zhibai Formation comprises garnet-bearing gneisses containing sporadic boudins of high-pressure granulite, with estimated peak metamorphic temperature-pressure conditions of ~850 °C and 14-18 kbar (Zhong and Ding, 1996; Liu and Zhong, 1997; Ding and Zhong, 1999; Booth et al., 2009). The age of peak metamorphism for the high-pressure granulites has been variably estimated from ~40 Ma to ~24 Ma (Ding et al., 2001; Liu et al., 2007; Xu et al., 2010; Zhang et al., 2010b; Su et al., 2012). The Duoxiongla Complex comprises migmatitic gneisses and orthogneisses with protolith ages ranging from 1.6 Ga to 1.8 Ga, as determined by U-Pb zircon dating (Guo et al., 2008; Zhang et al., 2012c). The Paixiang Formation is composed of felsic gneisses with subordinate diopside and forsterite-bearing marbles (Geng et al., 2006). All units from the Namche Barwa Complex are intruded by Neogene granitoids with ages of ~13-3 Ma (Burg et al., 1998; Ding et al., 2001; Booth et al., 2004).

The IYS unit separates the Himalaya unit (Indian plate) to the south from the Lhasa unit (Asian plate) to the north (Fig.1). It forms a continuous zone, 2-10 km wide, consisting of highly deformed and metamorphosed sedimentary and ultramafic-mafic rocks, the latter representing a Neo-Tethyan ophiolite (Geng et al., 2006). In the EHS, the geochemistry of the IYS mafic rocks indicate a back-arc basin affinity (Geng et al., 2006), comparable to mafic rocks that crop out to the west at Xigaze and Zedang. Clinopyroxene $^{40}Ar/^{39}Ar$ dating for the IYS mafic rocks yielded a crystallization age of 200±4 Ma (Geng et al., 2004).

The Lhasa unit includes the Nyingchi Complex, the Bomi Complex, Paleozoic-Mesozoic cover strata, and abundant Mesozoic-Cenozoic granites (Fig.1). The Nyingchi Complex comprises gneisses, mica schists, marbles and minor granulites. These rocks have experienced upper amphibolite-facies metamorphism, locally rising to granulite grade (Zhang et al., 2010b; Zhang et al., 2010c). Detrital zircon age data suggest that the maximum depositional age of the Nyingchi Complex is no older than 490 Ma (Zhang et al., 2008; Dong et al., 2010). The Bomi Complex is exposed over the northern and eastern margin of the EHS, and has been interpreted to represent the Precambrian metamorphic basement of the Lhasa terrane (Dewey et al., 1988; Zheng et al., 2003). According to geological mapping (Zheng et al., 2003), the Bomi Complex can be divided into three subunits: (1) the lower Bomi Complex, consisting of gneisses, migmatites, mica schists, amphibolites and minor marbles; (2) the middle Bomi Complex that is composed of granite gneisses, biotite gneisses, migmatites and amphibolites; and (3) the upper Bomi Complex that is dominated by biotite gneisses. The metamorphic *P-T* conditions for the Bomi Complex were estimated at 3-8 kbar and 575-640 °C (Zheng et al., 2003) or at ~10.8 kbar and ~840 °C (Booth et al., 2009). Recently, using U-Pb dating on zircons from metamorphosed sedimentary and igneous rocks, Xu et al. (2013) established that the lower Bomi Complex is a quite young formation and represents a residual forearc basin, sourced from denudation of the Gangdese magmatic arc during the India-Asia continental collision. It was subducted during the Late Eocene and subjected to amphibolite-facies metamorphism at ~37 Ma.

The Lhasa unit granites were mostly emplaced during two intrusive episodes: ~133-110 Ma and ~66-57 Ma (Booth et al., 2004; Booth et al., 2009; Chiu et al., 2009; Zhang et al., 2010a; Guo et al., 2011). Chiu et al. (2009) suggested that the early Cretaceous granites probably formed in a post-collisional regime in response to the Late Jurassic-Early Cretaceous collision between the Qiangtang and Lhasa terrane. The Late Cretaceous-Paleocene granites resulted from northward Neo-Tethyan subduction during late Mesozoic time (Chiu et al., 2009; Guo et al., 2011). The Cretaceous-Paleocene granites were intruded by the later muscovite granites, two-mica granites and garnet-bearing granites, ranging from ~26-21 Ma in age (Ding et al., 2001; Chung et al., 2003; Booth et al., 2004; Zhang et al., 2010a; Guo et al., 2011; Pan et al., 2012). These Late Oligocene-Early Miocene granites resulted from partial melting of thickened lower crust (Chung et al., 2003; Zhang et al., 2010a).

2.2. Sample description and protolith discrimination

Samples used in this study were collected near the road between Bomi and Motuo (Fig.1). The granite gneisses in the Bomi Complex are generally light grey in color, whereas the biotite gneisses are dark grey (Fig.2). The granite gneisses are intruded by the biotite gneisses. They are variably migmatized and their leucosomes form concordant to nearly concordant veins. The leucosomes were avoided during sampling. Four granite gneiss samples were collected from the Bomi Complex. The granite gneisses are composed of K-feldspar (~30-40%), quartz (~25-30%), plagioclase (~10-15%), biotite (~13-15%), and muscovite (~3-5%), with minor amounts of zircon and Fe-Ti oxides (Fig.3a, b). The mineral composition of the gneisses suggests that their protolith is granite. Three biotite gneiss samples were interbedded with granite gneisses. The biotite gneisses contain quartz (~32-38 %), plagioclase (~30-35%), biotite (~20-25%), K-feldspar (~5-8%), muscovite (~1-2%), and accessory xenotime and zircon (Fig.3c, d). The mineral composition indicates that the protoliths of the biotite gneisses are probably the intrusive rocks. Together with zircon morphology and geochemical data (see below) indicate that the biotite gneiss is a meta-tonalite.

3. Analytical methods

3.1. Zircon U-Pb dating

Zircons were separated by heavy-liquid and magnetic methods and then purified by hand picking under a binocular microscope. Zircon crystals were mounted in an epoxy disc and then were polished. Cathodoluminescence (CL) imaging was carried out using a Quanta 400FEG environmental scanning electron microscope equipped with an Oxford energy dispersive spectroscopy system and a Gatan CL3+ detector at the State Key Laboratory of Continental Dynamics, Northwest University, Xi'an, China. The operating conditions for the CL imaging were at 15 kV and 20 nA. Typical CL images were obtained to characterize each grain in terms of size, growth morphology, and internal structure, and were used to guide analytical spot selection for U-Pb dating and Lu-Hf analysis.

Zircon U-Pb dating and trace element analyses were conducted synchronously by LA-ICP-MS at the State Key Laboratory of Geological Processes and Mineral Resources (GPMR), China University of Geosciences, Wuhan, China. Detailed operating conditions for the laser ablation system and the ICP-MS instrument and data reduction are the same as description by Liu et al. (2008a; 2010a; 2010b). Laser sampling was performed using a GeoLas 2005. An Agilent 7500a ICP-MS instrument was used to acquire ion-signal intensities. Helium was applied as a carrier gas. Argon was used as the make-up gas and mixed with the carrier gas via a T-connector before entering the ICP. Nitrogen was added into the central gas flow (Ar+He) of the Ar plasma to decrease the detection limit and improve precision (Hu et al., 2008). The laser spot is 32 μm in diameter. Zircon 91500 was used as an external standard to normalize isotopic discrimination during analysis. NIST610 glass was used as an external standard to normalize U, Th, Pb and trace element concentrations of unknowns. The Agilent Chemstation was utilized for the acquisition of each individual analysis. Off-line selection and integration of background and analyte signals, and time-drift correction and quantitative calibration for trace element analyses and U-Pb dating were performed by *ICPMSDataCal* (Liu et al., 2010a). Uncertainties of individual analyses are reported at 1σ; weighted mean ages are calculated at 2σ level. Concordia diagrams and weighted mean calculations were made using Isoplot/Ex_ver3 (Ludwig, 2003).

3.2. Zircon Lu-Hf isotope analysis

In situ zircon Lu-Hf isotope measurements were undertaken using a Neptune Plus MC-ICP-MS (Thermo Fisher Scientific, Germany) in combination with a GeoLas 2005 excimer ArF laser ablation system (Lambda Physik, Göttingen, Germany) at the state Key Laboratory of GPMR. The energy density of laser ablation that was used in this study was 5.3 J cm^{-2}. Helium was used as the carrier gas within the ablation cell and was merged with argon (makeup gas) after the ablation cell. A simple Y junction downstream from the sample cell allowed the addition of small amounts of nitrogen (4 ml min^{-1}) to the argon makeup gas flow (Hu et al., 2008). Compared to the standard arrangement, the addition of nitrogen in combination with the use of the newly designed X skimmer cone and Jet sample cone in the Neptune Plus improved the signal intensity of Hf, Yb and Lu by a factor of 5.3, 4.0 and 2.4, respectively. The laser spot is 44 μm in diameter. Analytical spots were located close to or on the top of LA-ICP-MS spots or in the same growth domain as inferred from CL images. Zircons 91500, GJ-1, Mud Tank and Temora were analyzed as the reference standard. Detailed operating conditions for the laser ablation system and the MC-ICP-MS instrument and analytical method are the same as description by Hu et al. (2012).

The major limitation to accurate *in situ* zircon Hf isotope determination by LA-MC-ICP-MS is the large isobaric interference from ^{176}Yb and, to a much lesser extent, from ^{176}Lu on ^{176}Hf (Woodhead et al., 2004). It has been shown that the mass fractionation of Yb (β_{Yb}) is not constant over time and that the β_{Yb} that is obtained from the introduction of solutions is unsuitable for *in situ* zircon measurements (Woodhead et al., 2004). The under- or over-estimation of the β_{Yb} value would undoubtedly affect the accurate correction of ^{176}Yb and thus the determined ^{176}Hf/^{177}Hf ratio. We applied the directly obtained β_{Yb} value in real-time from the zircon sample itself. The ^{179}Hf/^{177}Hf and ^{173}Yb/^{171}Yb ratios were used to calculate the mass bias of Hf (β_{Hf}) and Yb (β_{Yb}), that were normalised to ^{179}Hf/^{177}Hf =0.7325 and ^{173}Yb/^{171}Yb=1.1248 (Blichert-Toft et al., 1997) using an exponential correction for mass bias. Interference of ^{176}Yb on ^{176}Hf was corrected by measuring the interference-free ^{173}Yb isotope and using ^{176}Yb/^{173}Yb =0.7876 (McCulloch et al., 1977) to calculate ^{176}Yb/^{177}Hf. Similarly, the relatively minor interference of ^{176}Lu on ^{176}Hf was corrected by measuring the intensity of the interference-free ^{175}Lu isotope and using the recommended ^{176}Lu/^{175}Lu =0.02656 (Blichert-Toft et al., 1997) to calculate ^{176}Lu/^{177}Hf. We used the mass bias of Yb (β_{Yb}) to calculate the mass fractionation of Lu because of their similar physicochemical properties. Off-line selection and integration of analyte signals, and mass bias calibrations were performed using *ICPMSDataCal* (Liu et al., 2010a). The decay constant for ^{176}Lu of 1.865×10^{-11} year^{-1} was adopted (Scherer et al., 2001). Initial ^{176}Hf/^{177}Hf ratio, denoted as ε_{Hf}(t), is calculated relative to the chondritic reservoir with a ^{176}Hf/^{177}Hf ratio of 0.282772 and ^{176}Lu/^{177}Hf of 0.0332 (Blichert-Toft et al., 1997). Single-stage Hf model ages (T_{DM1}) are calculated relative to the depleted mantle, which is assumed to have a linear isotopic growth from ^{176}Hf/^{177}Hf=0.279718 at 4.55 Ga to 0.283250 at present, with ^{176}Lu/^{177}Hf ratio of 0.0384 (Vervoort and Blichert-Toft, 1999), and two-stage Hf model ages (T_{DM2}) are calculated by assuming a mean $^{176}Lu/^{177}Hf$ value of 0.015 for the average continental crust (Griffin et al., 2002).

3.3. Whole-rock major and trace element analyses

Major elements were measured by XRF at the State Key Laboratory of GPMR. The analytical uncertainty is <5 %. Trace elements and rare earth elements (REE) were measured at the GPMR. About 50 mg of sample powders were digested by HF+HNO_3 in Teflon bombs and analyzed with an Agilent 7500a ICP-MS. The analytical precision is better than 5% for elements with concentrations >10 ppm, and less than 10% for those <10 ppm. The detailed analytical procedures are described in Liu et al. (2008b).

4. Results

4.1. Zircon U-Pb geochronology

Representative zircon CL images and U-Pb Concordia plots for zircons are shown in figures 4 and 5, respectively. LA-ICP-MS zircon U-Pb data are listed in the supplemental electronic data tables (Tables A).

4.1.1. Granite gneiss sample T844

Zircon crystals from the granite gneiss sample T844 are subhedral and transparent. They are 100-200 μm in length, with ratio of length to width ranging from 1.5:1 to 2:1. In CL images, zircon crystals commonly have oscillatory zoning (Fig. 4a), implying a magmatic genesis (Corfu et al., 2003). Many zircons exhibit an extremely narrow (<5 μm) outer rim with high CL intensity. The boundaries between the grey cores and the bright rims are often blurred. Twenty-one analyses were performed on twenty-one zircon grains. All of the analyses have moderate Th (45-211 ppm) and U (56-541 ppm) contents, with relatively high Th/U ratios of 0.28-0.82, consistent with their magmatic origin. Most zircons in this sample are concordant and few exhibit significant lead loss on the Concordia diagram (Fig. 5a). The resulting upper intercept age is 1347±27 Ma (MSWD=0.6). These zircons yielded $^{207}Pb/^{206}Pb$ ages between 1220±91 Ma and 1391±63 Ma, with a weighted mean of 1343±27 Ma (MSWD=0.3), identical to the upper intercept age within analytical error. Thus we interpret the weighted mean age of 1343±27 Ma to represent magma crystallization age of the protolith of the granite gneiss.

4.1.2. Granite gneiss sample T1063

Most zircons from the granite gneiss sample T1063 show prismatic crystals of variable length, but generally with rounded terminations. They have grain sizes of 150-250 μm in length, with ratios of length to width ranging from 2:1 to 3:1. In CL images, these zircon crystals commonly have oscillatory zoning (Fig. 4b), implying their magmatic origin (Corfu et al., 2003). Discontinuous narrow metamorphic rims can also be observed around some grains (Fig. 4b). Twenty-five analyses were obtained on twenty-five zircon grains. All of the analyses have moderate Th (45-344 ppm) and U (53-534 ppm) contents, with relatively high Th/U ratios of 0.29-1.15, consistent with their magmatic origin. Most zircons in this sample are concordant and some exhibit weak lead loss on the Concordia diagram (Fig. 5b). The resulting upper intercept age is 1281±20 Ma (MSWD=0.5). These zircons yielded $^{207}Pb/^{206}Pb$ ages between 1231±45 Ma and 1377±67 Ma, with a weighted mean of 1276±22 Ma (MSWD=0.4), identical to the upper intercept age within analytical error. Thus we interpreted the weighted mean age of 1276±22 Ma to represent the magma crystallization age of the protolith of the granite gneiss.

4.1.3. Biotite gneiss sample T843

Zircon crystals from the biotite gneiss sample T843 are subhedral, transparent and light yellow in colour. They are 100-150 μm in length, with ratio of length to width ranging from 2:1 to 3:1. In CL images, these zircon crystals commonly have planar zoning (Fig. 4c), implying crystallization from an intermediate magma (Corfu et al., 2003). Discontinuous narrow light rims can be observed around some grains (Fig. 4c). Eighteen analyses were performed on eighteen zircon grains. The zircons have Th abundances of 367-2480 ppm, U abundances of 607-2520 ppm, and Th/U ratios of 0.60-1.10, consistent with their magmatic origin. Some zircons in this sample exhibit significant lead loss and are discordant on the Concordia diagram (Fig. 5c). The resulting upper intercept age is 1267±15 Ma (MSWD=0.4). These zircons yielded $^{207}Pb/^{206}Pb$ ages between 1187±43 Ma and 1277±40 Ma, with a weighted mean of 1251±16 Ma (MSWD=0.3), identical to the upper intercept age within analytical error. We interpreted the age of 1251±16 Ma to represent the magma crystallization age of the protolith of the biotite gneiss.

4.1.4. Biotite gneiss sample T1062

Zircon crystals from the biotite gneiss sample T1062 show short to long prismatic crystals, but generally have rounded terminations. They have grain sizes of 200-350 μm in length, with ratios of length to width ranging from 2.5:1 to 4:1. In CL images, these zircon crystals commonly have weak planar zoning (Fig. 4d), implying crystallization from an intermediate magma (Corfu et al., 2003). Twenty-five analyses were done on twenty-five zircon grains. The zircons have Th of 84-2024 ppm, U of 225-1387 ppm, and Th/U ratios of 0.29-1.46. Most zircons in this sample exhibit significant lead loss and most analyses are discordant on the Concordia diagram (Fig. 5d). The resulting upper intercept age is 1275±25 Ma (MSWD=1.1). These zircons yielded $^{207}Pb/^{206}Pb$ ages between 1181±39 Ma and 1367±50 Ma, with a weighted mean of 1250±18 Ma (MSWD=1.0), identical to the upper intercept age within analytical error. The age of 1250±18 Ma represents the magma crystallization age of the protolith of the biotite gneiss.

4.2. Whole-rock major and trace element compositions

Whole-rock major and trace element data for both the gneiss samples are given in the supplemental electronic data tables (Table B). The granite gneisses are highly siliceous, with SiO_2 ranging from 71.71% to 73.08%. They have high contents of alkalis, with K_2O=3.27-6.0% and Na_2O=3.12-4.91%, and total K_2O+Na_2O varies from 8.18% to 9.12%, with K_2O/Na_2O=0.67-1.92. They have low abundances of $Fe_2O_3^{tot}$ (1.87-2.64%), MgO (0.48-0.82%), CaO (0.59-1.23%) and TiO_2 (0.21-0.26%). Al_2O_3 contents range from 14.02% to 15.05%. Mg numbers range from 37.0 to 43.7. The granite gneisses are weakly-strongly peraluminous with A/CNK values of 1.07-1.13. In Ab-An-Or ternary diagram (Fig.6), these gneisses plot in granite field. The major element composition of the granite gneisses is similar to that of aluminous A-type granite, as defined by King et al. (1997). The granite gneisses also share the features common to aluminous A-type granites in terms of trace element geochemistry. They are characterized by high 10,000×Ga/Al ratios ranging from 2.74 to 2.85, and all samples fall in field of A-type granites in discrimination diagrams (Fig.7). The sum of the Zr, Nb, Ce, and Y contents is greater than 370 ppm, of which the Zr contents are between ~205 ppm and ~373 ppm. The granite gneisses are also enriched in REE with total concentrations of 250-399 ppm. Chondrite-normalized REE patterns (Fig.8a) of these granite gneisses invariably show relative enrichment of light rare earth elements (LREE) with high $(La/Yb)_N$ ratios of 11.3-30.0 and moderate negative Eu anomalies (Eu/Eu*=0.44-0.57). On the primitive mantle-normalized spider diagram (Fig. 8b), they show negative anomalies of Ba, Nb, Ta, Sr, P and Ti, consistent with the patters of A-type granites (Wu et al., 2002). Overall, these geochemical characteristics show that the protoliths of the granite gneisses are probably aluminous A-type granites.

In contrast to the granite gneisses, the biotite gneisses have lower SiO_2 (63.87-67.69%), K_2O (1.78-2.70%), total alkalis contents (K_2O+Na_2O=6.29-7.40%), and K_2O/Na_2O ratios (0.39-0.57). But they display higher Al_2O_3 (15.99-16.17%), $Fe_2O_3^{tot}$ (3.77-5.40%), MgO (1.72-3.19%), CaO (2.05-3.31%) and TiO_2 (0.43-0.56%). The biotite gneisses are weakly-strongly peraluminous with A/CNK values of 1.05-1.11. In Ab-An-Or ternary diagram (Fig.6), these biotite gneisses straddle the tonalite and the trondhjemite fields. The biotite gneisses have lower REE contents relative to the granite gneisses (Fig. 8a), but also display enrichment of LREE relative to heavy rare elements (HREE) with $(La/Yb)_N$ ratios of 10.1-28.3 and weakly negative Eu anomalies (Eu*/Eu=0.78-0.83). On the primitive mantle-normalized spider diagram (Fig. 8b), they also show negative anomalies of Ba, Nb, Ta, Sr, P and Ti, but with higher Sr, P, Ti and lower Ba, Nb abundances compared with the granite gneisses.

4.3. Zircon Lu-Hf isotope compositions

Lu-Hf isotopic data for zircons from both the granite gneiss samples (T844, T1063) and the biotite gneiss samples (T843 and T1062) are given in the supplemental electronic data tables (Table C). Variations in Hf isotope ratios $\varepsilon_{Hf}(t)$ with their U-Pb ages (t) are plotted in Fig. 9.

Twelve Lu-Hf analyses were obtained on twelve dated zircon grains from the granite gneiss sample T844. $^{176}Hf/^{177}Hf$ ratios range from 0.282009 to 0.282086 (Table C). Assuming t=1340 Ma, the calculated $\varepsilon_{Hf}(t)$ values range from +1.8 to +4.0, with a weighted mean of +2.4±0.4

(MSWD=3.1). Their two-stage Hf model ages (T_{DM2}) range from 1858±49 Ma to 1993±59 Ma, with a weighted mean of 1960±24 Ma (MSWD=0.8) (Fig. 10a).

Twelve Lu-Hf analyses were obtained on twelve dated zircon grains from the granite gneiss sample T1063. They have $^{176}Hf/^{177}Hf$ ratios of 0.281995 to 0.282076 (Table C). Assuming t=1280 Ma, the calculated $\varepsilon_{Hf}(t)$ values range from +0.5 to +2.6, with a weighted mean of +1.2±0.5 (MSWD=4.5). Their T_{DM2} ages range from 1902±45 Ma to 2049±47 Ma, with a weighted mean of 1985±26 Ma (MSWD=1.1) (Fig. 10b).

Fourteen Lu-Hf analyses were undertaken on fourteen dated zircon grains from the biotite gneiss sample T843. $^{176}Hf/^{177}Hf$ ratios range from 0.282169 to 0.282261 (Table C). Assuming t=1250 Ma, the calculated $\varepsilon_{Hf}(t)$ values range from +3.5 to +8.4, with a weighted mean of +5.8±0.6 (MSWD=13). Their T_{DM2} ages range from 1511±43 Ma to 1763±29 Ma, with a weighted mean of 1675±37 Ma (MSWD=3.3) (Fig. 10c).

Twelve Lu-Hf analyses were undertaken on twelve dated zircon grains from the biotite gneiss sample T1062, of which one analysis has relatively higher $^{176}Hf/^{177}Hf$ ratio of 0.282359, corresponding to ε_{Hf}(1250 Ma) value of +10.5±0.3 and T_{DM2} age of 1383±38 Ma. The remaining analyses yielded $^{176}Hf/^{177}Hf$ ratios of 0.282176 to 0.282303 (Table C). Assuming t=1250 Ma, the calculated $\varepsilon_{Hf}(t)$ values range from +5.7 to +8.5, with a weighted mean of +6.7±0.6 (MSWD=6.8). Their T_{DM2} ages range from 1506±62 Ma to 1683±44 Ma, with a weighted mean of 1621±25 Ma (MSWD=1.7) (Fig. 10d).

5. Discussion

5.1. The oldest magmatism in the Lhasa terrane

The oldest published ages from basement rocks of the Lhasa terrane are from Neoproterozoic gneisses (920-800 Ma) from the Amdo basement in northern Lhasa subterrane (Guynn et al., 2006; Guynn et al., 2011; Zhang et al., 2012b). In the central Lhasa subterrane, the reported oldest rocks are the ~787-748 Ma granitoids and gabbros from the just west of Nam Tso Lake (Hu et al., 2005); these have experienced an amphibolite-facies to granulite-facies metamorphism during the Late Neoproterozoic at ~680-650 Ma (Dong et al., 2011; Zhang et al., 2012a). In the present study, the zircons from both the granite gneiss samples (T844 and T1063) show oscillatory zoning, and high Th/U ratios, which are typical for magmatic zircons (Corfu et al., 2003). Furthermore, these zircons have relatively high REE contents and distinctly fractionated REE patterns, with enrichment in HREE and depletion of LREE (Fig. S1 in supplementary materials), typical of magmatic zircons (Hoskin and Schaltegger, 2003). The zircons in the two granite gneiss samples yielded weighted mean $^{207}Pb/^{206}Pb$ ages of 1343±27 Ma (2σ; MSWD=0.3) and 1276±22 Ma (2σ; MSWD=0.4), respectively, which are interpreted as the formation ages of the granite gneiss protoliths from the Bomi Complex. In addition, the zircons from two biotite gneiss samples (T843 and T1062) show planar zoning, high Th/U ratios, relatively high REE contents and distinctly fractionated REE patterns, with enrichment in HREE and depletion of LREE (Fig. S1 in supplementary materials), which are also typical for magmatic zircons (Corfu et al., 2003; Hoskin and Schaltegger, 2003). These zircons in the two biotite gneiss samples gave an identical weighted mean $^{207}Pb/^{206}Pb$ age of ~1250 Ma, interpreted as a third magmatic event in the Bomi Complex. Thus the Lhasa terrane has experienced at least three intrusive phases during the Mesoproterozoic. To our knowledge, both the granite gneisses and the biotite gneisses are the oldest rocks identified from the Lhasa terrane.

A great many detrital zircons with Mesoproterozoic ages have been reported from the Paleozoic metasedimentary rocks in the Lhasa terrane (Zhu et al., 2011a). These detrital zircons show a distinctive age population of ~1170 Ma. In the apparent absence of igneous zircons of

Mesoproterozoic age prior to this study these grains were assumed to be exotic, and specifically to have been derived from the Albany-Fraser belt in southwest Australia (Zhu et al., 2011a). In the light of the results of the present study, the Mesoproterozoic magmatism had happened in the Lhasa terrane. Though the magmatic zircon ages obtained in this study are older than the distinctive age population of ~1170 Ma, we suggest that these Mesoproterozoic detrital zircons could be derived (at least partly) from the Lhasa terrane itself. Recently, Gehrels et al. (2011) also published large numbers of detrital zircon ages from different portions of the Tibet-Himalayan orogen. Their results show that both the Lhasa terrane and Tethyan Himalaya have similar age distributions. Hence, the Lhasa terrane is interpreted to have originated along the northern margin of the India during Paleozoic time (Gehrels et al., 2011). This simplifies the paleographic reconstruction of the region because it obviates the necessity to displace the Lhasa terrane to the northwestern margin of Australia during the Paleozoic as proposed by Zhu et al. (2011a).

The Bomi Complex in the EHS could be comparable to the basement beneath the central Lhasa subterrane as has been previously assumed (Zhang et al., 2007b; Zhu et al., 2009; Zhu et al., 2011b). The central Lhasa subterrane, which is separated from the Gangdese subterrane by the Luobadui-Milashan Fault to the south and the northern Lhasa subterrane by the Shiquanhe-Nam Tso Mélange Zone to the north (Fig.12), is composed of a Carboniferous-Permian metasedimentary sequence, a lower Cretaceous volcano-sedimentary sequence and associated granitoids with minor Ordovician, Silurian, and Triassic limestones (Pan et al., 2004; Zhu et al., 2009; Zhu et al., 2011b) and rare Neoproterozoic basement (Hu et al., 2005; Dong et al., 2011; Zhang et al., 2012a). While the Gangdese and northern Lhasa subterrane is characterized by juvenile crust, the central Lhasa subterrane is assumed to represent a microcontinent underlain by Archean and Proterozoic basement (Zhu et al., 2009; Zhu et al., 2011b). This hypothesis is supported by the following four lines of evidence. These are: (1) the whole-rock Nd model ages of 0.9-3.2 Ga for Meso-Cenozoic siliciclastic and igneous rocks (Kapp et al., 2005; Chu et al., 2006; Zhang et al., 2007b; Zhu et al., 2009); (2) the zircon Hf crustal model ages of 1.0-2.6 Ga for the Meso-Cenozoic igneous rocks (Zhu et al., 2009; Zhu et al., 2011b) ; (3) the inherited zircon U-Pb ages of 1032-2877 Ma from the Permian-Jurassic granites (Chu et al., 2006; Zhu et al., 2011b); and (4) the detrital zircon ages of 980-3323 Ma from the Paleozoic metasedimentary rocks (Leier et al., 2007; Zhu et al., 2011a) that could be soured from denudation of the Lhasa basement exposed previously. Although with Archean material information, the central Lhasa subterrane is characterized by an important Late Paleoproterozoic-Mesoproterozoic period of crustal growth, consistent with the evolution of the Bomi Complex. Thus the Bomi Complex and its equivalent beneath the central Lhasa subterrane constitute the basement of Lhasa that extend in an east-west direction for >1000 km.

5.2. Petrogenesis

The origin of A-type granites is still a subject of active discussion, mainly because so many compositional variants have been found (Bonin, 2007). Although several processes may be involved in their generation , the major debate concerns their source regions and the role of the mantle during their formation (Wu et al., 2002). A number of petrogenetic schemes have been proposed for the magma sources of A-type granites, which fall into two categories, involving crust and mantle sources, while a few advocate mixing between crust and mantle sources (Schmitt et al., 2000; Kemp and Hawkesworth, 2003; Bonin, 2007; Zhang et al., 2007a). According to the above discussion, the protoliths of the granite gneisses in the Bomi Complex are aluminous A-type granites. Based on the mineralogical and geochemical similarities between the aluminous A-type granites and the felsic I-type granites in the Lachlan Fold Belt, King et al. (1997) point to that aluminous A-type granites are generally produced by partial melting of felsic intercrustal sources as the I-type granites. The major difference between petrogenetic schemes for the aluminous A-type magmas and the I-type magmas is that different physical conditions prevailed (King et al., 1997). The higher temperature is required to produce aluminous A-type granites relative to the I-type granites (King et al., 1997). Zr saturation temperatures were calculated after Watson & Harrison (1983) for these granite gneiss samples in the Bomi Complex. The resulted temperatures are between 815 ℃ and 867 ℃. Because these gneisses are poor in inherited zircons, the calculated zircon saturation temperatures are underestimations of their initial temperature. The magma temperatures therefore are higher than the general I-type granite magmas. We therefore favor that the magmas of the gneiss protoliths had derived by direct partial melting of middle to lower crustal felsic igneous rocks. Because the Hf model ages record crustal residence time since its extraction from the depleted mantle, the T_{DM2} can be used as proxies for the minimum source ages of host magma from which the zircon crystallized (Zheng et al., 2006). Although the two granitic magmas show different emplace times, they have identical T_{DM2} ages of ~2.0 Ga (Fig. 10a, b), indicating both the two magmas derived from a common source. The T_{DM2} age of ~2.0 Ga suggests that the Lhasa terrane may be underlain by Lower Proterozoic basement. In binary Nb versus Y diagram (Fig. 11), the gneiss samples plot dominantly in the field of 'Within-Plate' granitoids and straddle into the arc granitoids (Pearce et al., 1984). Moreover, A-type granitic magma is generally accepted to reflected lithospheric extension (Whalen et al., 1987). Thus the high temperatures required to produce the protracted magmatism in the Lhasa terrane may have been initiated by mantle upwelling or mafic magma influx into a localized area in a continuous extensional setting.

The analyzed samples for the biotite gneisses fall in the field of the sub-alkaline series. In Ab-An-Or ternary diagram (Fig.6), these biotite gneisses straddle the tonalite and the trondhjemite fields. Together the petrologic features, we consider that the biotite gneiss protoliths were probably tonalites. These biotite gneiss samples have variable REE contents but similar chondrite-normalized REE patterns with moderately enriched light REE, relatively unfractionated heavy REE. They have weak negative Eu anomalies (Fig. 8a). Such REE characteristics are similar to arc-related magmas of intermediate compositions. The primitive mantle normalized trace element patterns show generally similar shapes for all samples (Fig. 8b). They are characteristized by a relative enrichment in LILEs (Rb, Th and U) and LREEs (La, Ce, and Pr), but a depletion in Nb, Ta, Sr, and Ti, which are similar to those of arc granitoids (Zhou et al., 2002). The biotite gneiss samples plot into the 'Volcanic Arc' granitoid field in the Y versus Nb tectonic discriminant diagram (Fig. 11), compared to the granite gneisses in the Bomi Complex that plots within the 'Within Plate' field. Calculated zircon saturation temperatures (741-777 □) for the biotite gneiss samples are lower than those of the granite gneisses, consistent with those of the 'wet' granitoids formed in a subduction setting. The two dated biotite gneiss samples have zircon $\varepsilon_{Hf}(t)$ values of +8.1 to +3.6 and +10.5 to +5.7, respectively, indicating magmatism with a dominantly juvenile mantle contribution. The Hf isotope features are similar to those of the Late Cretaceous granitoids in the Lhasa terrane that formed in continental arc setting (Ji et al., 2009). Our evidence suggests that the protoliths of the biotite gneisses are typical calc-alkaline granitoids, and their formation would be related to a subduction process.

5.3. Geodynamic processes

In the Lhasa terrane, the magma crystallization ages (~1340-1280 Ma) of the aluminous A-type granites are older than those (~1250 Ma) of the tonalites. There are two possible interpretations for the obtained data. Firstly, although the former had formed in a 'Within Plate' setting while the latter in an arc setting, both of them could be formed in an active continental margin. Considering the petrological, geochemical and geochronological studies presented above, we invoke a model of a continuous arc through this period to explain the magma evolution of the Lhasa terrane during the Mesoproterozoic. When earlier extension developing in a back-arc setting, direct mantle-derived heat or basaltic magmas produced from decompressed asthenosphere advect into the extending region, causing partial melting of preexisting arc crust and forming the aluminous A-type granites. The earlier development of crustal extension (thinning) was replaced by convergence and subduction as the regional stress field evolved into compression. The fluids from the dehydrating slab had infiltrated into the overlying mantle wedge and juvenile lower crust (the underplating mafic rocks), causing initiation of arc magmatism. The resulted magmas had intruded into the previous aluminous A-type granites.

The second interpretation is that the aluminous A-type granites mark an earlier Mesoproterozoic rift. The rift can be correlated to the final breakup of the supercontinent Columbia and have opened an ocean. The subsequent subduction of ocean slab had led to initiation of arc magmatism at ~1250 Ma. The Grenvillian (1.3-1.0 Ga) orogenic and subduction related events have been regarded as a critical linkage in Rodinia reconstruction (Dalziel, 1991; Hoffman, 1991; Moores, 1991). The newly recognized Mesoproterozoic arc-related magmatism in the Lhasa could represent the accretion at convergent margin before the continental collision. Both of the accretion and collision constitute the Grenvillian orogeny, causing the assembly of the Rodina supercontinent.

We prefer the latter interpretation given that the Lhasa terrane have originated the northern margin of India (Yin and Harrison, 2000). The geological record in the Lhasa terrane during the Mesoproterozoic is comparable with the southeastern India, although more geological constraints are needed. In southeastern Peninsular India, there are several deformed alkaline complexes outcrop near the contact zone between the Eastern Ghats Belt and the Archaean cratons. U-Th-Pb zircon dating constrains the intrusion of the alkaline magmas to a narrow period between ~1262 and ~1480 Ma (Upadhyay, 2008; and references therein). Upadhyay (2008) interpreted the alkaline complexes to record a Mesoproterozoic rift correlated to the breakup of the supercontinent Columbia. The rifting along the eastern proto-Indian margin and the opening of an ocean may be related to the separation of India from east Antarctica. Finally, the rift basin or ocean basin had closed at the late Mesoproterozoic during Rodinia assembly (Upadhyay, 2008).

6. Conclusions

The protoliths of the granite gneisses and biotite gneisses from the Bomi Complex in the Lhasa terrane were possibly granites and tonalites, respectively. The protoliths of the granite gneisses were emplaced at ~1343 Ma and ~1276 Ma, while the protoliths of the biotite gneisses at ~1250 Ma. Thus the basement of the Lhasa terrane is Mesoproterozoic, which could provide source materials for the Paleozoic metasedimentary rocks in the Lhasa terrane. Geochemical characteristics show that the granite gneisses have an aluminous A-type granite affinity. These granite gneiss protoliths were produced by protracted high temperature partial melting of a common felsic intercrustal source in a possible rift setting related to the breakup of supercontinent Columbia. In contrast, the biotite gneiss protoliths have similar geochemical characteristics to those of arc granitoids that formed in a subduction-related process during Rodinia assembly. The Bomi Complex thus may be related to the contact zone between the Eastern Ghats Belt and the Archaean cratons in southeastern India during Mesoproterozoic.

Acknowledgments

This research is supported by the Natural Science Foundation of China (grants: 41103019 and 41073046), the National Key Project for Basic Research (No.2011CB403102), China Geological Survey (No.1212011121261), and the Fundamental Research Funds for the Central Universities. We thank two anonymous reviewers for the constructive comments that greatly improved this manuscript.

References

Barker, F., 1979. Trondhjemites, Dacites and Related Rocks. Elsevier, Amsterdam.

Beck, R.A., Burbank, D.W., Sercombe, W.J., Riley, G.W., Barndt, J.K., Berry, J.R., Afzal, J., Khan, A.M., Jurgen, H., Metje, J., Cheema, A., Shafique, N.A., Lawrence, R.D., Khan, M.A., 1995. Stratigraphic evidence for an early collision between northwest India and Asia. Nature 373, 55-58.

Blichert-Toft, J., Chauvel, C., Albarède, F., 1997. Separation of Hf and Lu for high-precision isotope analysis of rock samples by magnetic sector-multiple collector ICP-MS. Contributions to Mineralogy and Petrology 127, 248-260.

Bonin, B., 2007. A-type granites and related rocks: Evolution of a concept, problems and prospects. Lithos 97, 1-29.

Booth, A.L., Chamberlain, C.P., Kidd, W.S.F., Zeitler, P.K., 2009. Constraints on the metamorphic evolution of the eastern Himalayan syntaxis from geochronologic and petrologic studies of Namche Barwa. Geological Society of America Bulletin 121, 385-407.

Booth, A.L., Zeitler, P.K., Kidd, W.S.F., Wooden, J., Liu, Y.P., B., I., Hern, M., Chamberlain, C.P., 2004. U-Pb zircon constraints on the Tectonic evolution of southeastern Tibet, Namche Barwa area. American Journal of Science 304, 889-929.

Burg, J.-P., Nievergelt, P., Oberli, F., Seward, D., Davy, P., Maurin, J.-C., Diao, Z., Meier, M., 1998. The Namche Barwa syntaxis: evidence for exhumation related to compressional crustal folding. Journal of Asian Earth Sciences 16, 239-252.

Burg, J., Davy, P., Nievergelt, P., Oberli, F., Seward, D., Diao, Z., Meier, M., 1997. Exhumation during crustal folding in the Namche-Barwa syntaxis. Terra Nova 9, 53-56.

Chiu, H.Y., Chung, S.L., Wu, F.Y., Liu, D.Y., Liang, Y.H., Lin, I.-J., Iizuka, Y., Xie, L.W., Wang, Y.B., Chu, M.F., 2009. Zircon U-Pb and Hf isotopic constraints from eastern Transhimalayan batholiths on the precollisional magmatic and tectonic evolution in southern Tibet. Tectonophysics 477, 3-19.

Chu, M.F., Chung, S.L., Song, B.A., Liu, D.Y., O'Reilly, S.Y., Pearson, N.J., Ji, J.Q., Wen, D.J., 2006. Zircon U-Pb and Hf isotope constraints on the Mesozoic tectonics and crustal evolution of southern Tibet. Geology 34, 745-748.

Chung, S.L., Chu, M.F., Zhang, Y.Q., Xie, Y.W., Lo, C.H., Lee, T.Y., Lan, C.Y., Li, X.H., Zhang, Q., Wang, Y.Z., 2005. Tibetan tectonic evolution inferred from spatial and temporal variations in post-collisional magmatism. Earth-Science Reviews 68, 173-196.

Chung, S.L., Liu, D.Y., Ji, J.Q., Chu, M.F., Lee, H.Y., Wen, D.J., Lo, C.H., Lee, T.Y., Qian, Q., Zhang, Q., 2003. Adakites from continental collision zones: Melting of thickened lower crust beneath southern Tibet. Geology 31, 1021-1024.

Corfu, F., Hanchar, J., Hoskin, P., Kinny, P., 2003. Atlas of Zircon Textures. Reviews in Mineralogy and Geochemistry 53, 469-500.

Dalziel, I., 1991. Pacific margins of Laurentia and East Antarctica-Australia as a conjugate rift pair: evidence and implications for an Eocambrian supercontinent. Geology 19, 598-601.

de Sigoyer, J., Chavagnac, V., Blichert-Toft, J., Villa, I.M., Luais, B., Guillot, S., Cosca, M., Mascle, G., 2000. Dating the Indian continental subduction and collisional thickening in the northwest Himalaya: Multichronology of the Tso Morari eclogites. Geology 28, 487-490.

Dewey, J., Shackleton, R., Chengfa, C., Yiyin, S., 1988. The tectonic evolution of the Tibetan Plateau. Philosophical Transactions of the Royal Society of London. Series A, Mathematical and Physical Sciences 379-413.

Ding, L., Zhong, D., 1999. Metamorphic characteristics and geotectoinc implications of the high-pressure granulites from Namjagbarwa, eastern Tibet. Science in China (Earth sciences) 42, 491-505.

Ding, L., Zhong, D.L., Yin, A., Kapp, P., Harrison, T.M., 2001. Cenozoic structural and metamorphic evolution of the eastern Himalayan syntaxis (Namche Barwa). Earth and Planetary Science Letters 192, 423-438.

Dong, X., Zhang, Z.M., Santosh, M., 2010. Zircon U-Pb chronology of the Nyingtri Group,

southern Lhasa terrane, Tibetean Plateau: implications for Grenvillian and Pan-African provenance and Mesozoic-Cenozoic metamorphism. The Journal of Geology 118, 677-690.
Dong, X., Zhang, Z.M., Santosh, M., Wang, W., Yu, F., Liu, F., 2011. Late Neoproterozoic thermal events in the northern Lhasa terrrane, south Tibet: Zircon chronology and tectonic implications. Journal of Geodynamics 52, 389-405.
Gehrels, G., Kapp, P., DeCelles, P., Pullen, A., Blakey, R., Weislogel, A., Ding, L., Guynn, J., Martin, A., McQuarrie, N., 2011. Detrital zircon geochronology of pre-Tertiary strata in the Tibetan-Himalayan orogen. Tectonics 30, TC5016.
Geng, Q.R., Pan, G.T., Zheng, L.L., Chen, Z.L., Fisher, R.D., Sun, Z.M., Ou, C.S., Dong, H., Wang, X.W., Li, S., Lou, X.Y., Fu, H., 2006. The eastern Himalayan syntaxis: major tectonic domains, ophiolitic mélanges and geologic evolution. Journal of Asian Earth Sciences 27, 265-285.
Geng, Q.R., Pan, G.T., Zheng, L.L., Sun, Z.M., Qu, C.S., Dong, H., 2004. Petrological characteristics and original settings of the Yarlung Tsangpo ophiolitic mélange, Namche Barwa, SE Tibet. Chinese Journal of Geology 39, 1-19 (in Chinese with English abstract).
Griffin, W.L., Wang, X., Jackson, S.E., Pearson, N.J., O'Reilly, S.Y., Xu, X., Zhou, X., 2002. Zircon chemistry and magma mixing, SE China: In-situ analysis of Hf isotopes, Tonglu and Pingtan igneous complexes. Lithos 61, 237-269.
Guo, L., Zhang, H.F., Harris, N., Pan, F.B., Xu, W.C., 2011. Origin and evolution of multi-stage felsic melts in eastern Gangdese belt: Constraints from U-Pb zircon dating and Hf isotopic composition. Lithos 127, 54-67.
Guo, L., Zhang, H.F., Xu, W.C., 2008. U-Pb zircon ages of migmatite and granitic gneiss from Duoxiongla in eastern Himalayan syntaxis and their geological implications. Acta Petrologica Sinica 24, 421-429 (in Chinese with English abstract).
Guynn, J., Kapp, P., Gehrels, G.E., Ding, L., 2011. U-Pb geochronology of basement rocks in central Tibet and paleogeographic implications. Journal of Asian Earth Sciences 43, 23-50.
Guynn, J., Kapp, P., Pullen, A., Heizler, M., Gehrels, G., Ding, L., 2006. Tibetan basement rocks near Amdo reveal "missing" Mesozoic tectonism along the Bangong suture, central Tibet. Geology 34, 505-508.
Hoffman, P., 1991. Did the breakout of Laurentia turn Gondwanaland inside-out? Science 252, 1409-1412.

Hoskin, P., Schaltegger, U., 2003. The composition of zircon and igneous and metamorphic petrogenesis. Reviews in Mineralogy and Geochemistry 53, 27-62.

Hu, D.G., Wu, Z.H., Jiang, W., Shi, Y.R., Ye, P.S., Liu, Q.S., 2005. SHRIMP zircon U-Pb age and Nd isotopic study on the Nyainqentanglha Group in Tibet. Science in China (Earth sciences) 48, 1377-1386.

Hu, Z.C., Gao, S., Liu, Y.S., Hu, S.H., Chen, H.H., Yuan, H.L., 2008. Signal enhancement in laser ablation ICP-MS by addition of nitrogen in the central channel gas. Journal of Analytical Atomic Spectrometry 23, 1093-1101.

Hu, Z.C., Liu, Y.S., Gao, S., Liu, W.G., Zhang, W., Tong, X.R., Lin, L., Zong, K.Q., Li, M., Chen, H.H., Zhou, L., Yang, L., 2012. Improved in situ Hf isotope ratio analysis of zircon using newly designed X skimmer cone and jet sample cone in combination with the addition of nitrogen by laser ablation multiple collector ICP-MS. Journal of Analytical Atomic Spectrometry 27, 1391-1399.

Ji, W.Q., Wu, F.Y., Chung, S.L., Li, J.X., Liu, C.Z., 2009. Zircon U-Pb geochronology and Hf isotopic constraints on petrogenesis of the Gangdese batholith, southern Tibet. Chemical Geology 262, 229-245.

Kapp, J., Harrison, T., Kapp, P., Grove, M., Lovera, O., Ding, L., 2005. Nyainqentanglha Shan: A window into the tectonic, thermal, and geochemical evolution of the Lhasa block, southern Tibet. Journal of Geophysical Research 110, B08413.

Kemp, A.I.S., Hawkesworth, C.J., 2003. Granitic perspectives on the generation and secular evolution of the continental crust. Treatise on Geochmestry 3, 349-410.

King, P.L., White, A.J.R., Chappell, B.W., Allen, C.M., 1997. Characterization and origin of aluminous A-type granites from the Lachlan Fold Belt, southeastern Australia. Journal of Petrology 38, 371-391.

Leech, M.L., Singh, S., Jain, A.K., Klemperer, S.L., Manickavasagam, R.M., 2005. The onset of India-Asia continental collision: Early, steep subduction required by the timing of UHP metamorphism in the western Himalaya. Earth and Planetary Science Letters 234, 83-97.

Leier, A.L., Kapp, P., Gehrels, G.E., DeCelles, P.G., 2007. Detrital zircon geochronology of Carboniferous-Cretaceous strata in the Lhasa terrane, Southern Tibet. Basin Research 19, 361-378.

Liu, Y., Yanc, Z.Q., Wang, M., 2007. History of zircon growth in a high-pressure granulite within the eastern Himalayan syntaxis, and tectonic implications. International Geology Review 49, 861-872.

Liu, Y., Zhong, D., 1997. Petrology of high-pressure granulites from the eastern Himalayan syntaxis. Journal of Metamorphic Geology 15, 451-466.

Liu, Y.S., Gao, S., Hu, Z.C., Gao, C.G., Zong, K.Q., Wang, D.B., 2010a. Continental and oceanic crust recycling-induced melt-peridotite interactions in the Trans-North China Orogen: U-Pb dating, Hf isotopes and trace elements in zircons of mantle xenoliths. Journal of Petrology 51, 537-571.

Liu, Y.S., Hu, Z.C., Gao, S., Günther, D., Xu, J., Gao, C.G., Chen, H.H., 2008a. In situ analysis of major and trace elements of anhydrous minerals by LA-ICP-MS without applying an internal standard. Chemical Geology 257, 34-43.

Liu, Y.S., Hu, Z.C., Zong, K.Q., Gao, C.G., Gao, S.X., J., Chen, H., 2010b. Reappraisement and refinement of zircon U-Pb isotope and trace element analyses by LA-ICP-MS. Chinese Science Bulletin 55, 1535-1546.

Liu, Y.S., Zong, K.Q., Kelemen, P.B., Gao, S., 2008b. Geochemistry and magmatic history of eclogites and ultramafic rocks from the Chinese continental scientific drill hole: Subduction and ultrahigh-pressure metamorphism of lower crustal cumulates. Chemical Geology 247, 133-153.

Ludwig, K.R. (2003). ISOPLOT 3.0: A Geochronological Toolkit for Microsoft Excel. Berkeley, Berkeley Geochronology Center, California.

McCulloch, M.T., Rosman, K.J.R., De Laeter, J.R., 1977. The isotopic and elemental abundance of ytterbium in meteorites and terrestrial samples. Geochimica et Cosmochimica Acta 41, 1703-1707.

Moores, E., 1991. Southwest US-East Antarctic (SWEAT) connection: a hypothesis. Geology 19, 425-428.

Pan, F.B., Zhang, H.F., Harris, N., Xu, W.C., Guo, L., 2012. Oligocene magmatism in the eastern margin of the east Himalayan syntaxis and its implication for the India-Asia post-collisional process. Lithos 154, 181-192.

Pan, G.T., Ding, J., Wang, L.Q., 2004. Geological map (1:1500000) of Qinghai-Xizang (Tibetan) Plateau and adjacent areas. Chengdu Cartographic Publising House, Chengdu 1-148 (in Chinese).

Pan, G.T., Wang, L.Q., Li, R.S., Yuan, S.H., Ji, W.H., Yin, F.G., Zhang, W.P., Wang, B.D., 2012. Tectonic evolution of the Qinghai-Tibet Plateau. Journal of Asian Earth Sciences 53, 3-14.

Pearce, J., Harris, N., Tindle, A., 1984. Trace element discrimination diagrams for the tectonic interpretation of granitic rocks. Journal of Petrology 25, 956-983.

Scherer, E., Munker, C., Mezger, K., 2001. Calibration of the lutetium-hafnium clock. Science 293, 683-687.

Schmitt, A.K., Emmermann, R., Trumbull, R.B., Buhn, B., Henjes-Kunst, F., 2000. Petrogenesis and $^{40}Ar/^{39}Ar$ geochronology of the Brandberg Complex, Namibia: evidence for a major mantle contribution in metaluminous and peralkaline granites. Journal of Petrology 41, 1207-1239.

Su, W., Zhang, M., Liu, X., Lin, J., Ye, K., 2012. Exact timing of granulite metamorphism in the Namche-Barwa, eastern Himalayan syntaxis: new constraints from SIMS U-Pb zircon age. International Journal of Earth Sciences 101, 239-252.

Sun, S.S., McDonough, W.F., 1989. Chemical and isotopic systematics of oceanic basalts: implications for mantle composition and processes. Geological Society, London: Special Publication 42, 313-345.

Upadhyay, D., 2008. Alkaline magmatism along the southeastern margin of the Indian shield: Implications for regional geodynamics and constraints on craton-Eastern Ghats Belt suturing. Precambrian Research 162, 59-69.

Vervoort, J.D., Blichert-Toft, J., 1999. Evolution of the depleted mantle: Hf isotope evidence from juvenile rocks through time. Geochimica et Cosmochimica Acta 63, 533-556.

Watson, E.B., Harrison, T.M., 1983. Zircon saturation revisited: temperature and composition effects in a variety of crustal magma types. Earth and Planetary Science Letters 64, 295-304.

Whalen, J.B., Currie, K.L., Chappell, B.W., 1987. A-type granites: geochemical characteristics, discrimination and petrogenesis. Contributions to Mineralogy and Petrology 95, 407-419.

Woodhead, J., Hergt, J., Shelley, M., Eggins, S., Kemp, R., 2004. Zircon Hf-isotope analysis with an excimer laser, depth profiling, ablation of complex geometries, and concomitant age estimation. Chemical Geology 209, 121-125.

Wu, F.Y., Sun, D.Y., Li, H.M., Jahn, B.M., Wilde, S.A., 2002. A-type granites in northeastern China: age and geochemical constraints on their petrogenesis. Chemical Geology 187, 143-173.

Xu, W.C., ZHang, H.F., Harris, N., Guo, L., Pan, F.B., 2013. Rapid Eocene erosion, sedimentation and burial in the eastern Himalayan syntaxis and its geodynamic significance. Gondwana Research 23, 715-725.

Xu, W.C., Zhang, H.F., Parrish, R., Harris, N., Guo, L., Yuan, H.L., 2010. Timing of granulite-facies metamorphism in the eastern Himalayan syntaxis and its tectonic implications. Tectonophysics 485, 231-244.

Xu, Z.Q., Cai, Z.H., Li, H.Q., Chen, F.Y., Tang, Z.M., 2008. Tectonics and fabric kinematics of the Namche Barwa terrane, Eastern Himalayan Syntaxis. Acta Geologica Sinica 24, 1463-1476 (in Chinese with English abstract).

Yin, A., 2006. Cenozoic tectonic evolution of the Himalayan orogen as constrained by along-strike variation of structural geometry, exhumation history, and foreland sedimentation. Earth-Science Reviews 76, 1-131.

Yin, A., Harrison, T.M., 2000. Geologic evolution of the Himalayan-Tibetan orogen. Annual Review of Earth and Planetary Sciences 28, 211-280.

Zhang, H.F., Harris, N., Guo, L.X., W.C., 2010a. The significance of Cenozoic magmatism from the western margin of the eastern syntaxis, southeast Tibet. Contributions to Mineralogy and Petrology 160, 83-98.

Zhang, H.F., Parrish, R.R., Zhang, L., Xu, W.C., Yuan, H.L., Gao, S., Crowley, Q.G., 2007a. A-type granite and adakitic magmatism association in Songpan-Garze fold belt, eastern Tibetan Plateau: Implication for lithospheric delamination. Lithos 97, 323-335.

Zhang, H.F., Xu, W.C., Zong, K.Q., Yuan, H.L., Harris, N., 2008. Tectonic evolution of metasediments from the Gangdise Terrane, Asian plate, eastern Himalayan syntaxis, Tibet. International Geology Review 50, 914-930.

Zhang, J.J., Ji, J.Q., Zhong, D.L., Ding, L., He, S.D., 2004. Structural pattern of eastern Himalayan syntaxis in Namjagbarwa and its formation process. Science in China (Earth sciences) 47, 138-150.

Zhang, K.J., Zhang, Y.X., Li, B., Zhong, L.F., 2007b. Nd isotopes of siliciclastic rocks from Tibet, western China: Constraints on provenance and pre-Cenozoic tectonic evolution. Earth and Planetary Science Letters 256, 604-616.

Zhang, Z.M., Dong, X., Liu, F., Lin, Y.H., Yan, R., He, Z.Y., Santosh, M., 2012a. The making of Gondwana: Discovery of 650 Ma HP granulites from the North Lhasa, Tibet. Precambrian Research 212-213, 107-116.

Zhang, Z.M., Dong, X., Liu, F., Lin, Y.H.Y., R., Santosh, M., 2012b. Tectonic evolution of the Amdo Terrane, Central Tibet: Petrochemistry and zircon U-Pb geochronology. The Journal of Geology 120, 431-451.

Zhang, Z.M., Dong, X., Santosh, M., Liu, F., Wang, W., Yiu, F.H., Z.Y., Shen, K., 2012c. Petrology and geochronology of the Namche Barwa Complex in the eastern Himalayan syntaxis, Tibet: Constraints on the origin and evolution of the north-eastern margin of the Indian Craton. Gondwana Research 21, 123-137.

Zhang, Z.M., Zhao, G.C., Santosh, M., Wang, J.L., Dong, X., Liou, J.G., 2010b. Two stages of granulite facies metamorphism in the eastern Himalayan syntaxis, south Tibet: petrology, zircon geochronology and implications for the subduction of Neo-Tethys and the Indian continent beneath Asia. Journal of Metamorphic Geology 28, 719-733.

Zhang, Z.M., Zhao, G.C., Santosh, M., Wang, J.L., Dong, X., Shen, K., 2010c. Late Cretaceous charnockite with adakitic affinities from the Gangdese batholith, southeastern Tibet: evidence for Neo-Tethyan mid-ocean ridge subduction? Gondwana Research 17, 615-631.

Zheng, L.L., Dong, H., Geng, Q.R., Liao, G.Y., Sun, Z.M., Lou, X.Y., Li, S., 2003. 1:250,000 geological report of Motuo District with geological map. Chengdu Institute of Geology and Mineral Resources unpublished (in Chinese).

Zheng, Y., Zhao, Z., Wu, Y., Zhang, S., Liu, X., Wu, F., 2006. Zircon U–Pb age, Hf and O isotope constraints on protolith origin of ultrahigh-pressure eclogite and gneiss in the Dabie orogen. Chemical Geology 231, 135-158.

Zhong, D.L., Ding, L., 1996. Discovery of high-pressure basic granulite in Namjagbarwa area, Tibet, China. Chinese Science Bulletin 41, 87-88.

Zhou, M.F., Yan, D.P., Kennedy, A.K., Li, Y.Q., Ding, J., 2002. SHRIMP U-Pb zircon geochronological and geochemical evidence for Neoproterozoic arc-magmatism along the western margin of the Yangtze Block, South China. Earth and Planetary Science Letters 196, 51-67.

Zhu, D.C., Mo, X.X., Niu, Y.L., Zhao, Z.D., Wang, L.Q., Liu, Y.S., Wu, F.Y., 2009. Geochemical investigation of Early Cretaceous igneous rocks along an east-west traverse throughout the central Lhasa Terrane, Tibet. Chemical Geology 268, 298-312.

Zhu, D.C., Zhao, Z.D., Niu, Y.L., Dilek, Y., Mo, X.X., 2011a. Lhasa terrane in southern Tibet came from Australia. Geology 39, 727-730.

Zhu, D.C., Zhao, Z.D., Niu, Y.L., Mo, X.X., Chung, S.L., Hou, Z.Q., Wang, L.Q., Wu, F.Y., 2011b. The Lhasa Terrane: Record of a microcontinent and its histories of drift and growth. Earth and Planetary Science Letters 301, 241-255.

Figure Captions

Fig.1. Sketch map of the eastern Himalayan syntaxis, showing sample location (modified after Zheng et al. (2003)). Inset shows the study area. Abbreviations: A=lower Bomi Complex; B=middle Bomi Complex; C=upper Bomi Complex.

Fig.2. Photographs showing the contact relationship between the granite gneiss (T1062) and the biotite gneiss (T1063).

Fig.3. Microstructures of (a) the granite gneiss T844, (b) the granite gneiss T1063, (c) the biotite gneiss T843 and (d) the biotite gneiss T1062. Bi=biotite, Kfs=K-feldspar, Ms=muscovite, Pl=plagioclase, Qz=quartz.

Fig.4. Representative cathodoluminescence images of zircons from (a) the granite gneiss T844, (b) the granite gneiss T1063, (c) the biotite gneiss T843, and (d) the biotite gneiss T1062. The smaller circles show LA-ICP-MS dating spots and corresponding apparent ages, and the larger circles show the locations of Lu-Hf isotope analysis and corresponding epsilon Hf values.

Fig.5. Concordia diagrams of LA-ICP-MS U-Pb dating for zircons from (a) the granite gneiss T844, (b) the granite gneiss T1063, (c) the biotite gneiss T843 and (d) the biotite gneiss T1062.

Fig.6. Normative albite (Ab)-anorthite (An)-orthoclase (Or) contents of both the granite gneisses (diamond) and the biotite gneisses (circle) from the Bomi Complex in the eastern Himalayan

syntaxis. The Ab-An-Or classification for silicic rocks is after Barker (1979).

Fig.7. A-type granite discrimination diagram (after Whalen et al., 1987). Diamonds are the granite gneisses; circles represent the biotite gneisses.

Fig.8. (a) Chondrite-normalized REE patterns; (b) primitive mantle-normalized element spider diagram. Normalizing values are from Sun and McDonough (1989).

Fig.9. Plots of ε_{Hf}(t) versus U-Pb age for studied samples from the Bomi Complex in the eastern Himalayan syntaxis.

Fig.10. Histogram of two-stage Hf modal ages for (a) the granite gneiss T844, (b) the granite gneiss T1063, (c) the biotite gneiss T843 and (d) the biotite gneiss T1062.

Fig.11. Nb versus Y tectonic discrimination diagram for the granite gneiss (diamond) and the biotite gneiss (circle) samples. Discriminations boundaries follow Pearce et al. (1984). ORG=oceanic ridge granite; Syn-COLG=syn-collision granite; VAG=volcanic-arc granite; WPG=within-plate granite.

Fig.12. Sketch tectonic map of the south Tibet (modified after Pan et al., 2011 and Zhu et al., 2011a), showing the tectonic subdivision of Lhasa terrane. Abbreviation: BNS=Bangong-Nujiang suture zone; IYS=Indus-Yarlung suture zone; SNMZ=Shiquan River-Nam Tso Mélange Zone; LMF=Luobadui-Milashan Fault.

Research Highlights

- Zircon U-Pb dating, geochemistry and Hf isotope composition for the Bomi Complex.
- The basement of the Lhasa terrane is Mesoproterozoic.
- The protoliths of the granite gneisses are aluminous A-type granites
- The protoliths of the biotite gneisses were related to a subduction process.
- The Lhasa terrane may be related to the southeastern India during Mesoproterozoic.

Figure 1

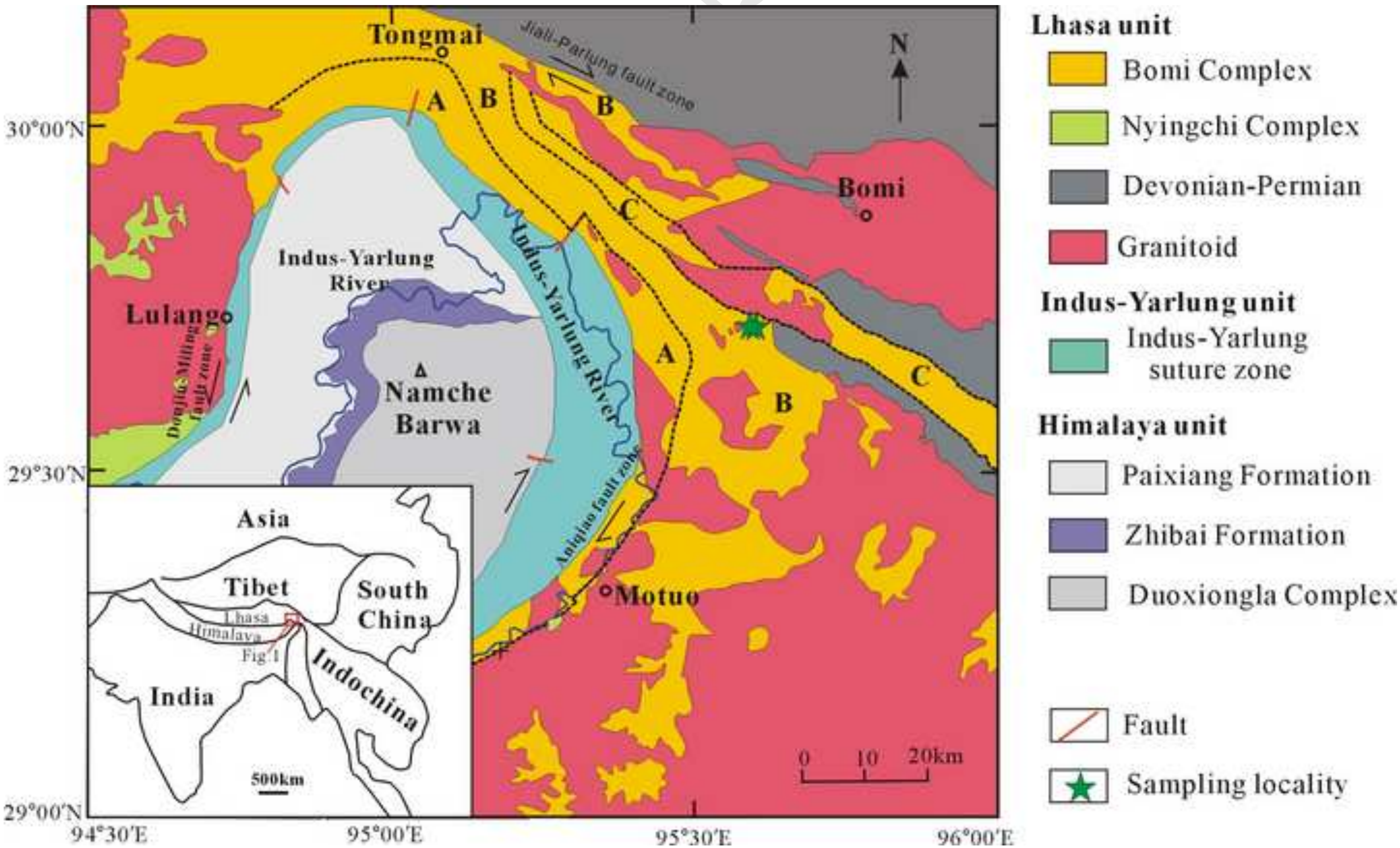

Tongmai
Jiali-Parlung fault zone
N
Bomi
Indus-Yarlung River
Lulang
Dongjiu-Milin fault zone
Namche Barwa
Indus-Yarlung River
Aniqiao fault zone
Motuo
30°00'N
29°30'N
29°00'N
94°30'E
95°00'E
95°30'E
96°00'E
0
10
20km
Asia
Tibet
South China
Lhasa
Himalaya
Fig.1
India
Indochina
500km
Lhasa unit
Bomi Complex
Nyingchi Complex
Devonian-Permian
Granitoid
Indus-Yarlung unit
Indus-Yarlung suture zone
Himalaya unit
Paixiang Formation
Zhibai Formation
Duoxiongla Complex
Fault
Sampling locality

Figure 2

Figure 3

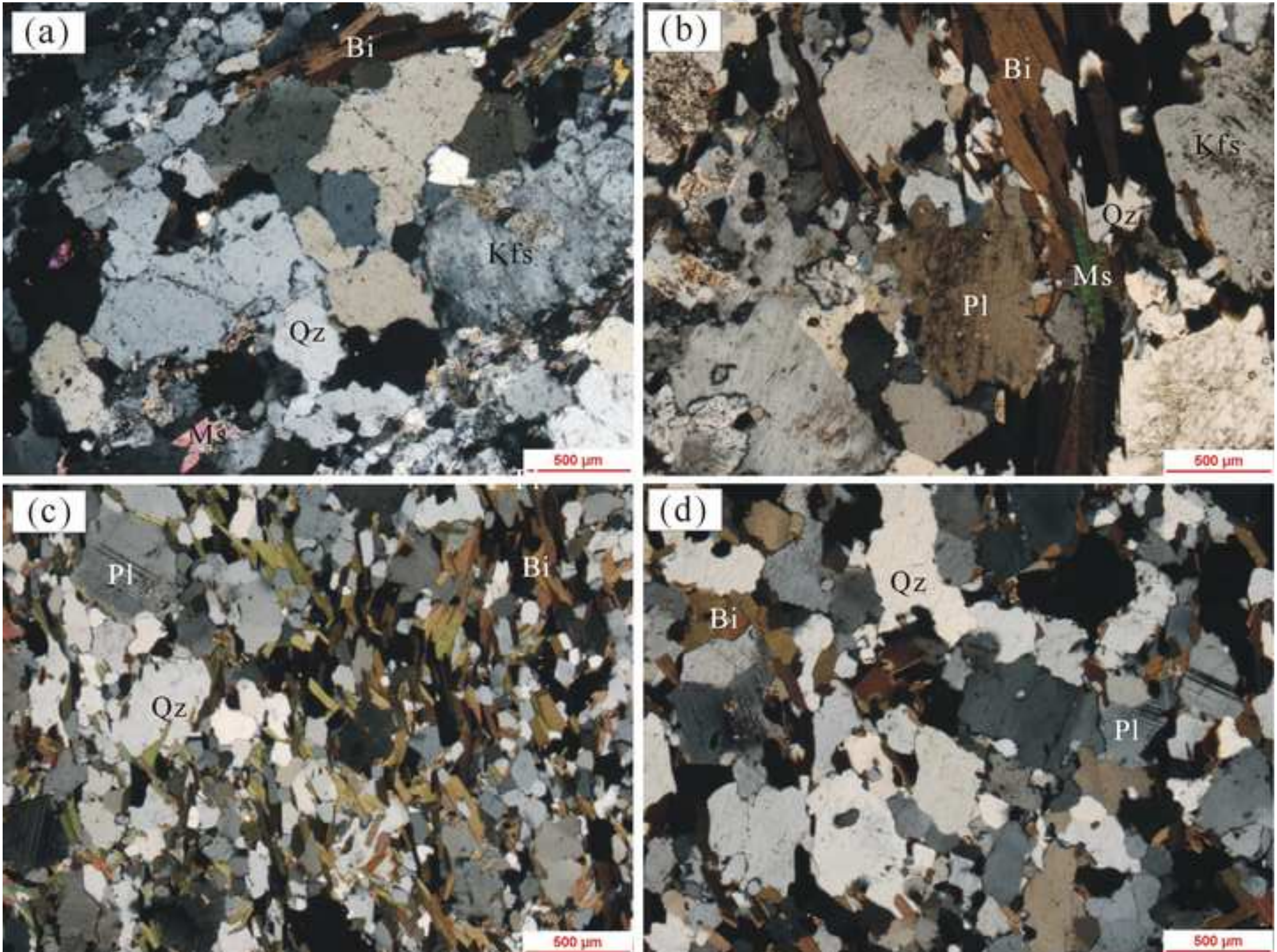
(a)
Bi
Kfs
Qz
Ms
500 µm
(b)
Bi
Kfs
Qz
Ms
Pl
500 µm
(c)
Pl
Bi
Qz
500 µm
(d)
Qz
Bi
Pl
500 µm

Figure 4

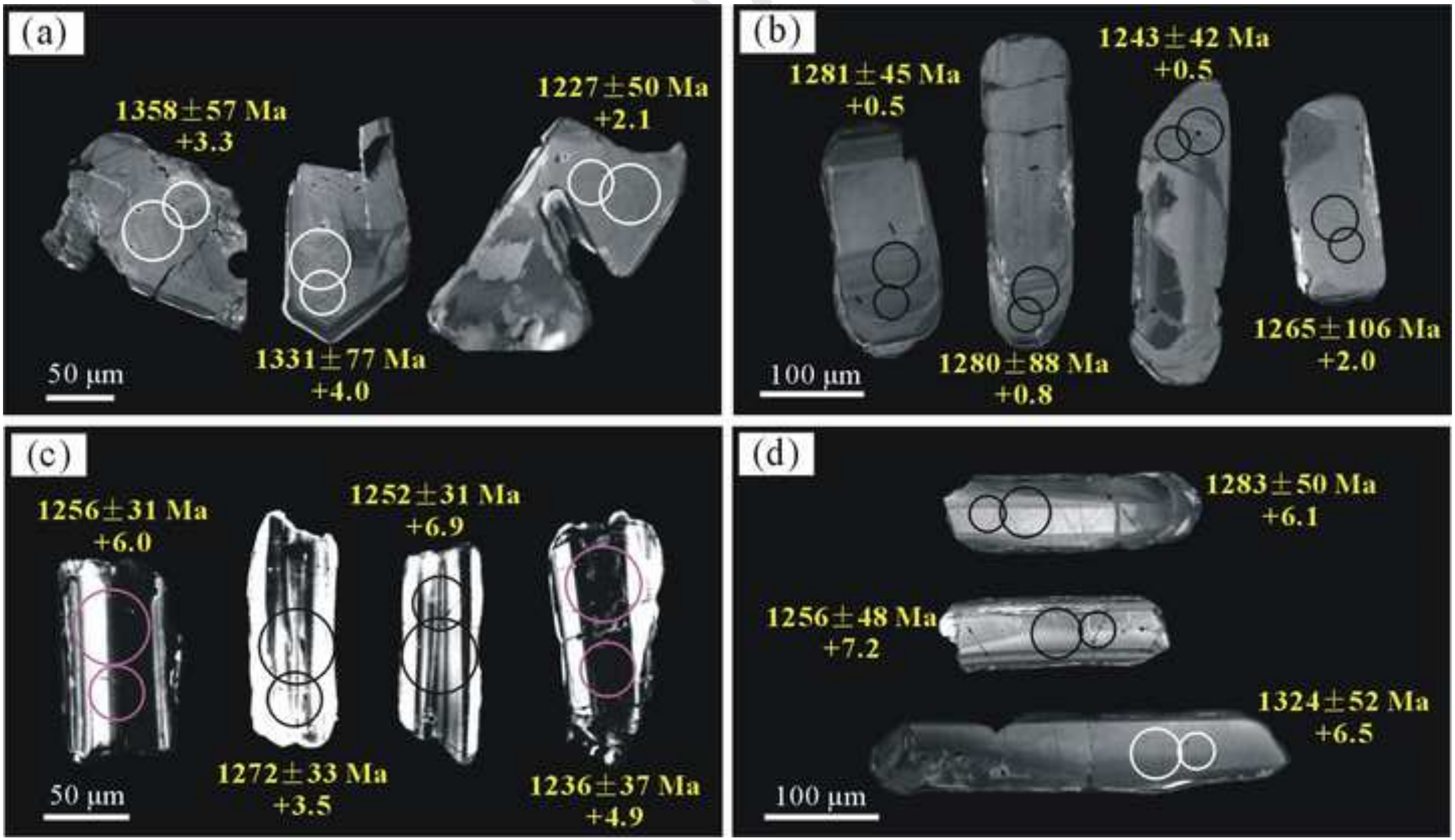

(a)
1358±57 Ma
+3.3
1331±77 Ma
+4.0
1227±50 Ma
+2.1
50 µm
(b)
1281±45 Ma
+0.5
1280±88 Ma
+0.8
1243±42 Ma
+0.5
1265±106 Ma
+2.0
100 µm
(c)
1256±31 Ma
+6.0
1272±33 Ma
+3.5
1252±31 Ma
+6.9
1236±37 Ma
+4.9
50 µm
(d)
1283±50 Ma
+6.1
1256±48 Ma
+7.2
1324±52 Ma
+6.5
100 µm

Figure 5

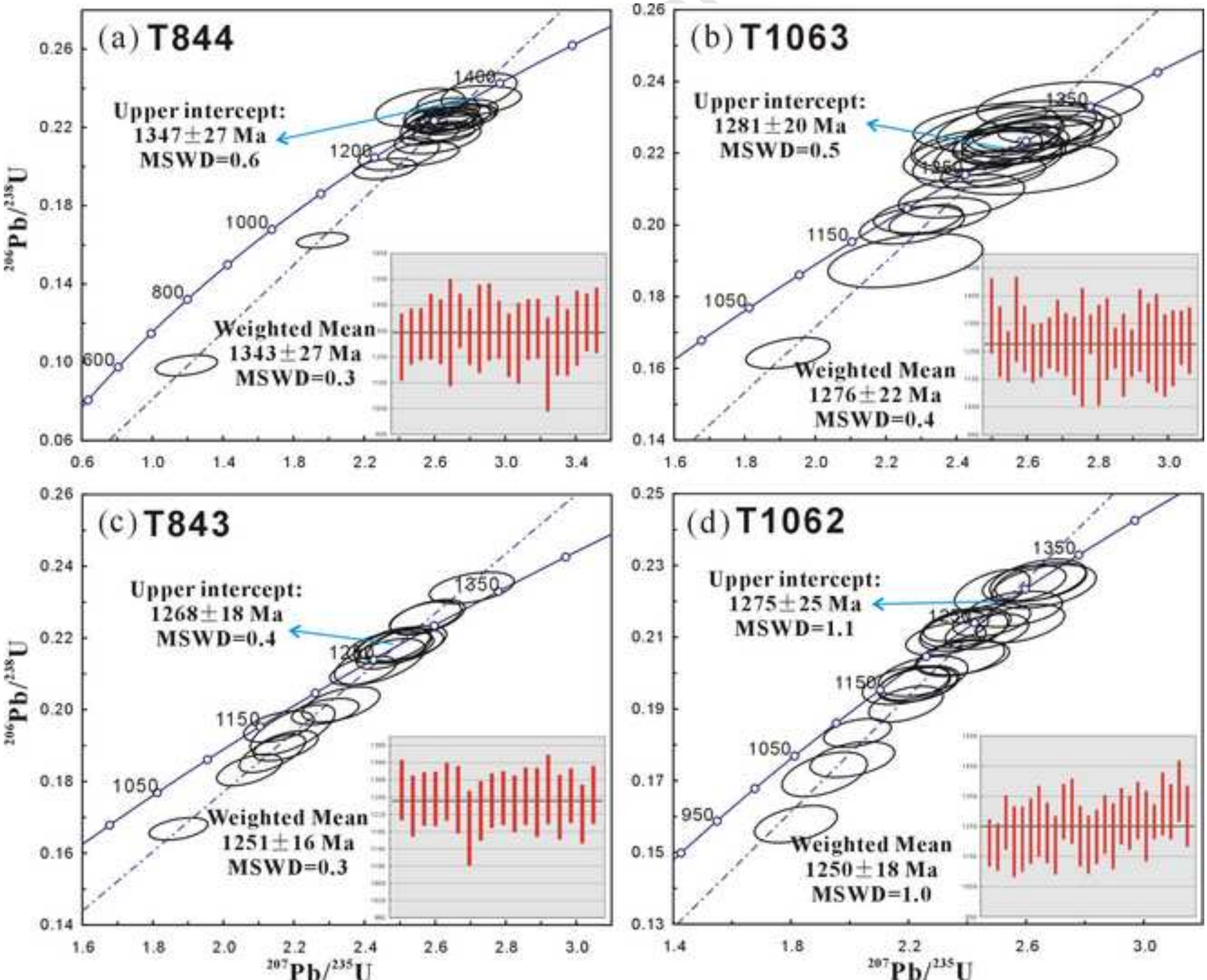
(a) T844
Upper intercept:
1347±27 Ma
MSWD=0.6
Weighted Mean
1343±27 Ma
MSWD=0.3
(b) T1063
Upper intercept:
1281±20 Ma
MSWD=0.5
Weighted Mean
1276±22 Ma
MSWD=0.4
(c) T843
Upper intercept:
1268±18 Ma
MSWD=0.4
Weighted Mean
1251±16 Ma
MSWD=0.3
(d) T1062
Upper intercept:
1275±25 Ma
MSWD=1.1
Weighted Mean
1250±18 Ma
MSWD=1.0
$^{206}Pb/^{238}U$
$^{207}Pb/^{235}U$

Figure 6

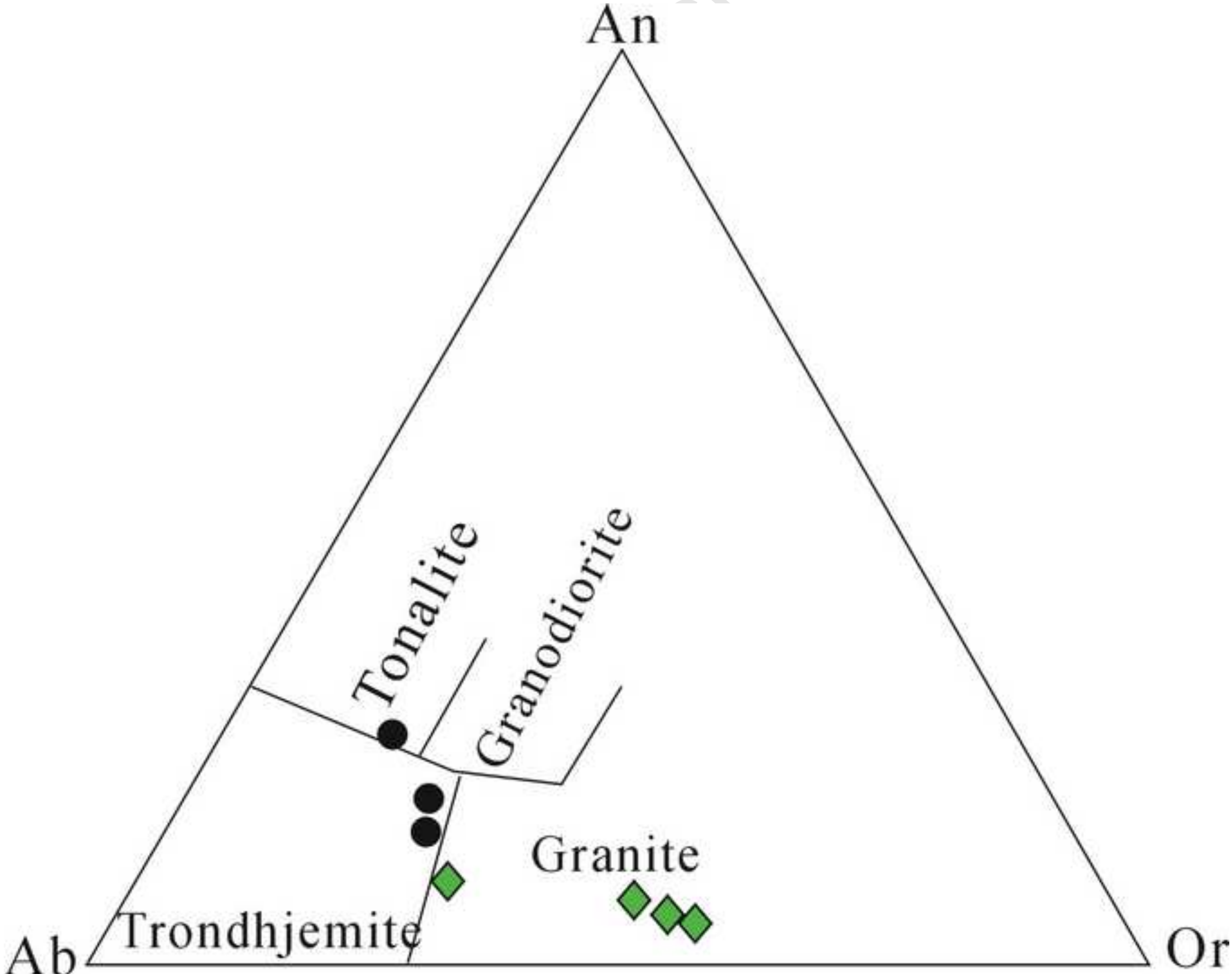

Figure 7

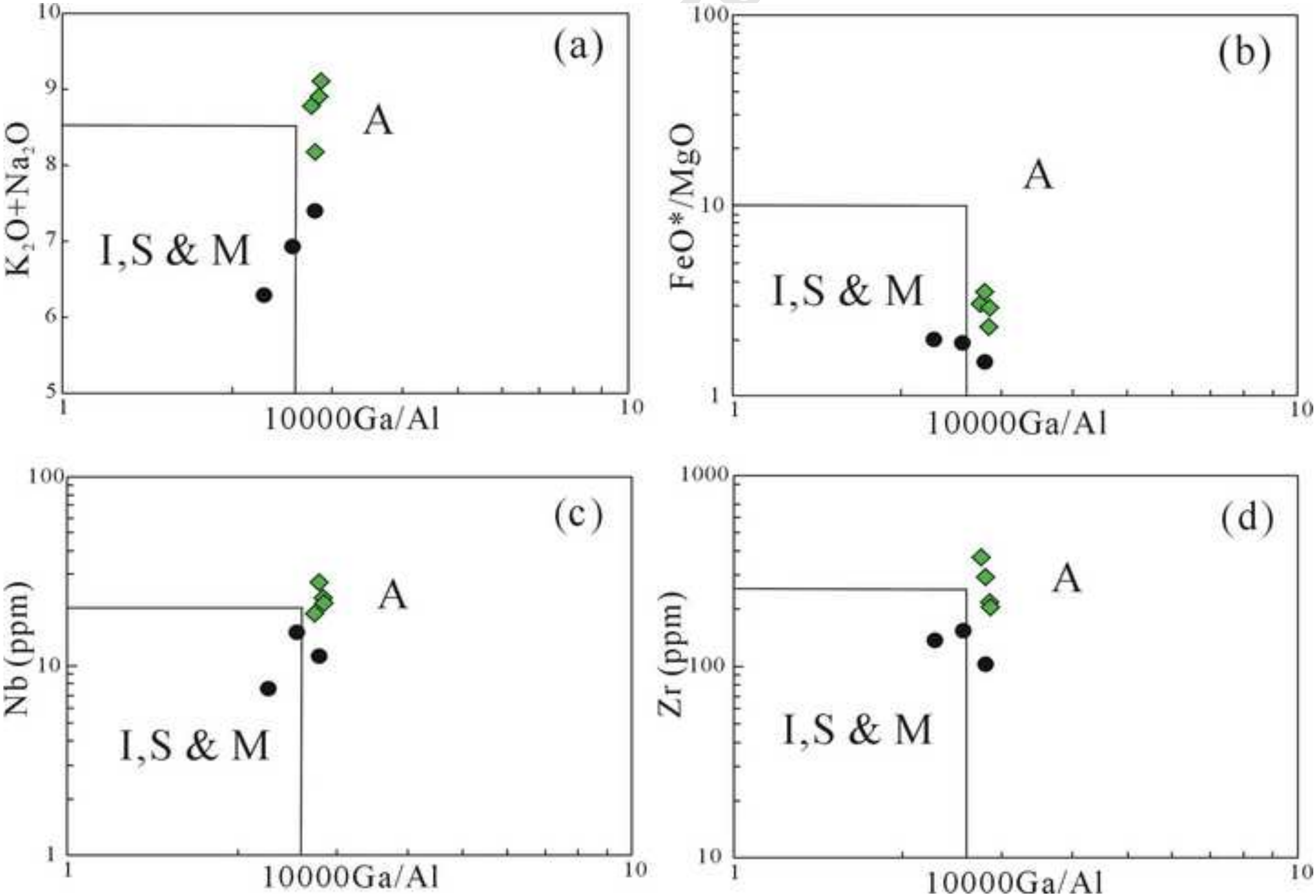

(a)
A
I,S & M
K_2O+Na_2O
10000Ga/Al
(b)
A
I,S & M
FeO*/MgO
10000Ga/Al
(c)
A
I,S & M
Nb (ppm)
10000Ga/Al
(d)
A
I,S & M
Zr (ppm)
10000Ga/Al

Figure 8

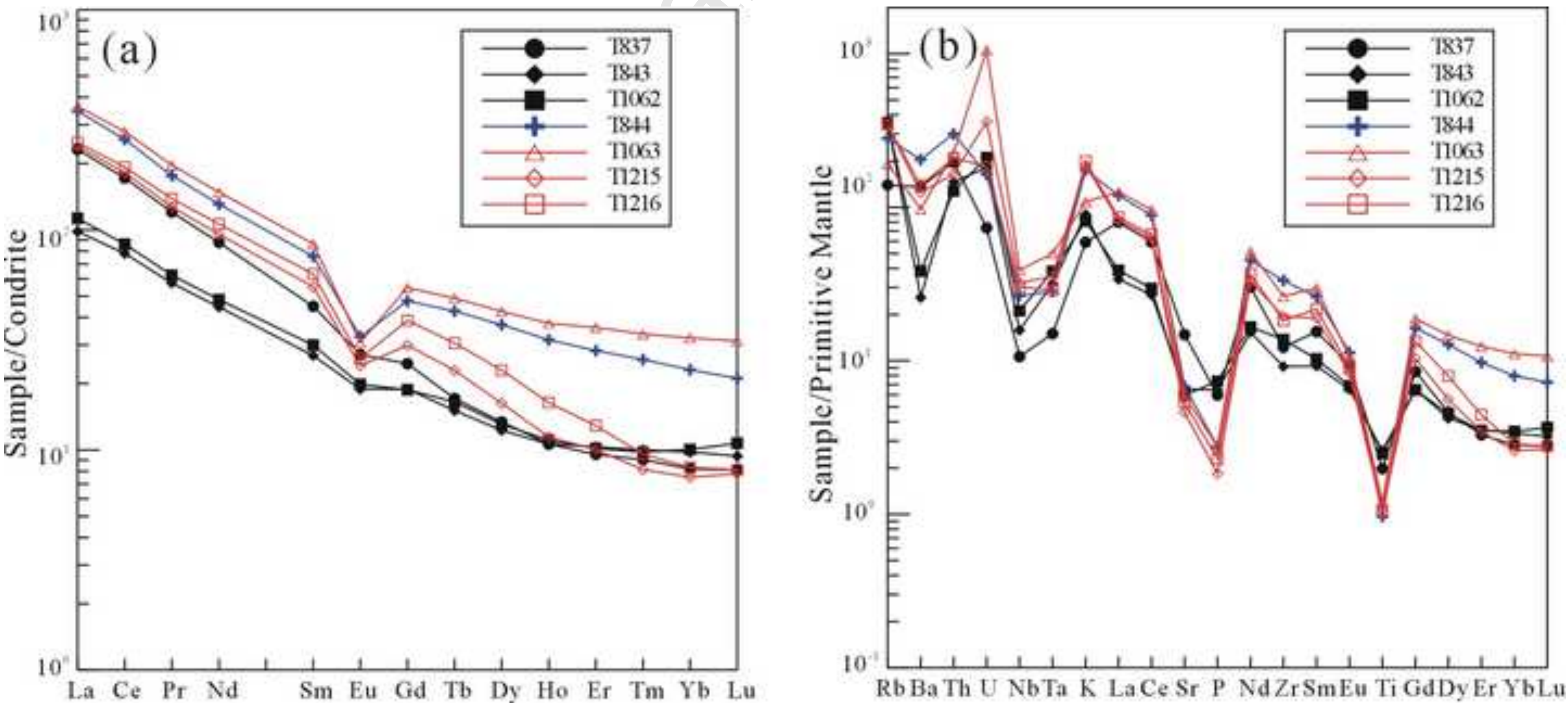
(a)
Sample/Condrite
La Ce Pr Nd Sm Eu Gd Tb Dy Ho Er Tm Yb Lu
T837
T843
T1062
T844
T1063
T1215
T1216
(b)
Sample/Primitive Mantle
Rb Ba Th U Nb Ta K La Ce Sr P Nd Zr Sm Eu Ti Gd Dy Er Yb Lu

Figure 9

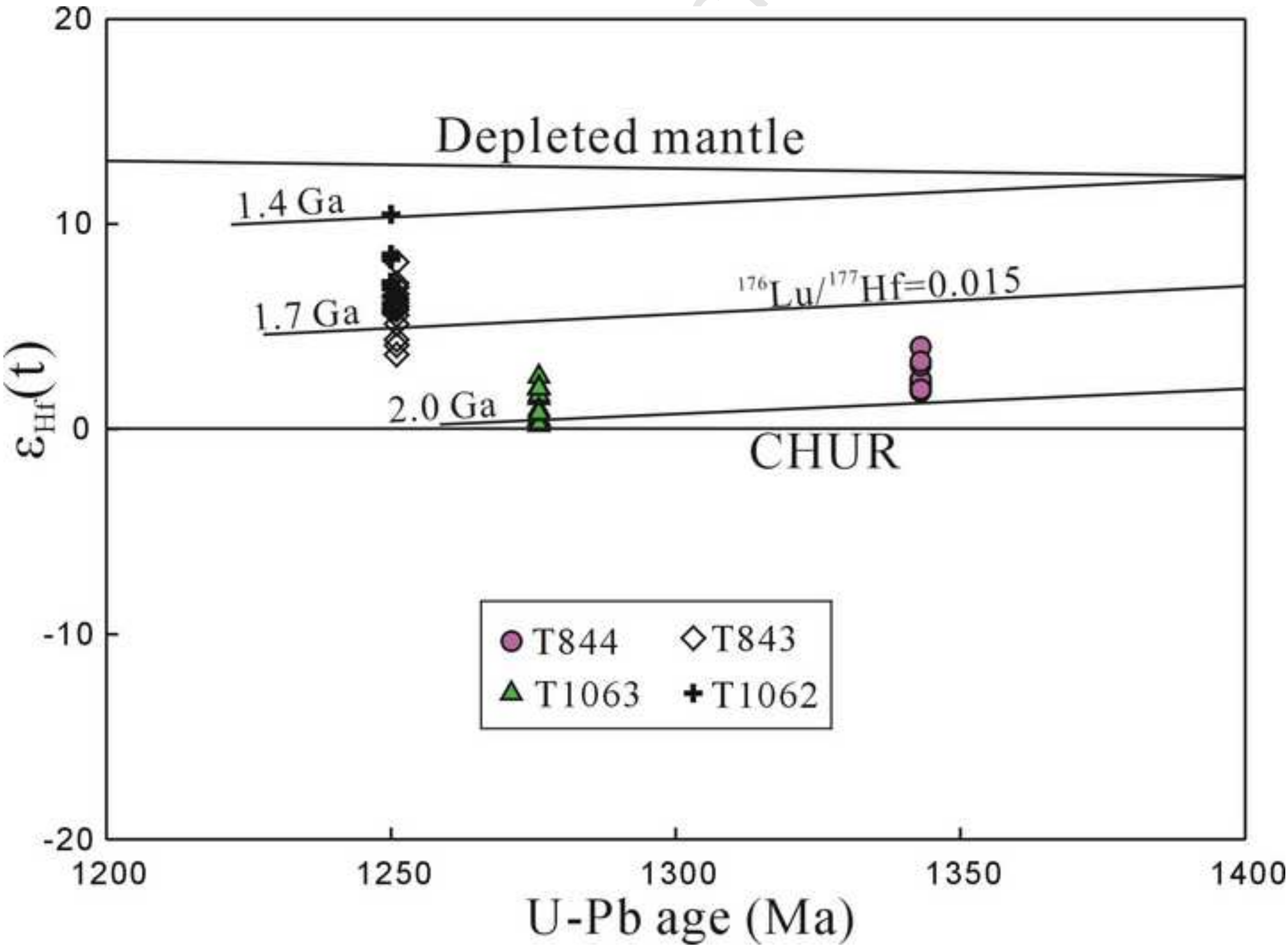
20
10
0
-10
-20
1200
1250
1300
1350
1400
U-Pb age (Ma)
$\varepsilon_{Hf}(t)$
Depleted mantle
1.4 Ga
1.7 Ga
2.0 Ga
$^{176}Lu/^{177}Hf=0.015$
CHUR
T844
T843
T1063
T1062

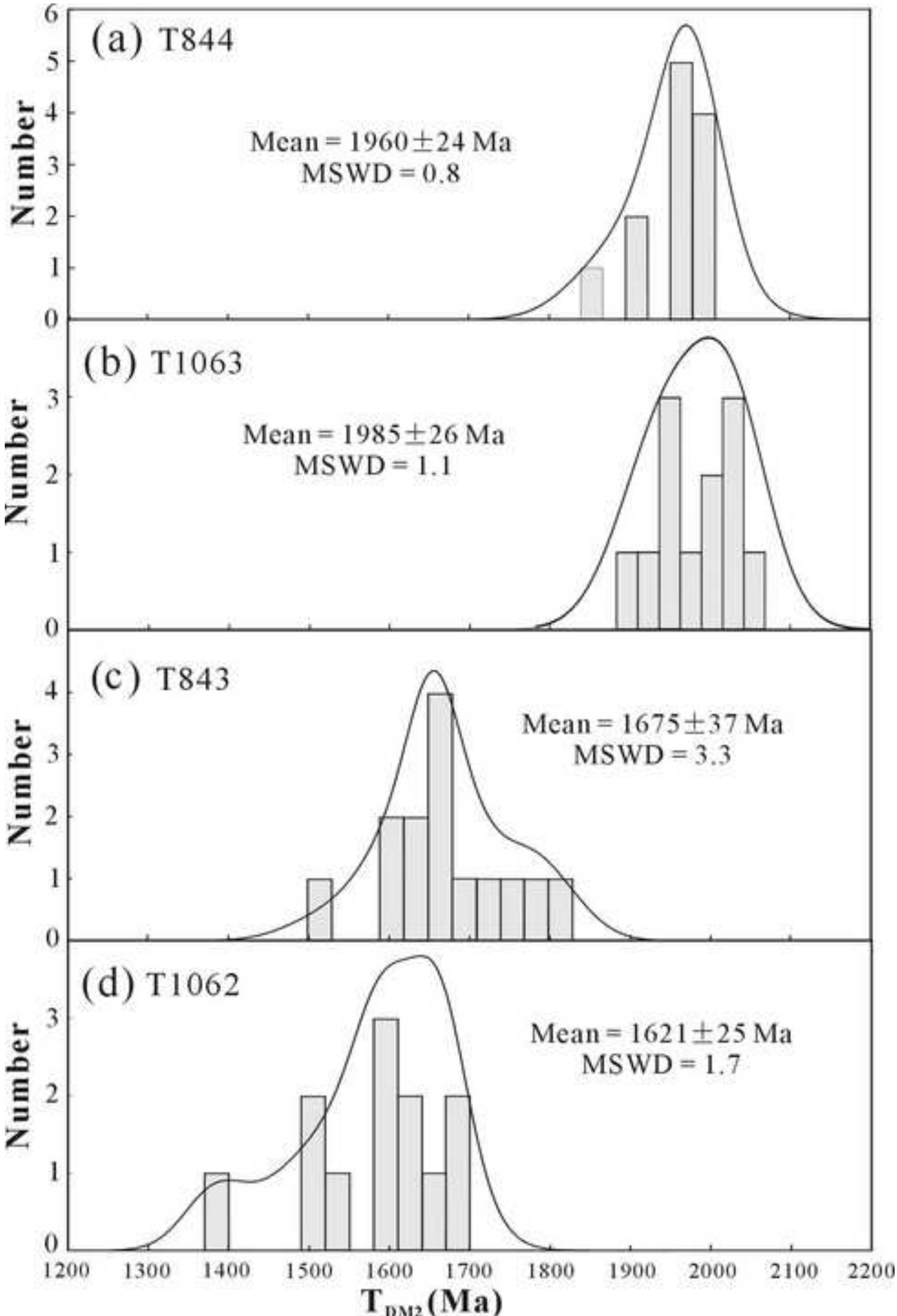
(a) T844
Mean = 1960±24 Ma
MSWD = 0.8
(b) T1063
Mean = 1985±26 Ma
MSWD = 1.1
(c) T843
Mean = 1675±37 Ma
MSWD = 3.3
(d) T1062
Mean = 1621±25 Ma
MSWD = 1.7
Number
T DM2 (Ma)
1200 1300 1400 1500 1600 1700 1800 1900 2000 2100 2200

Figure 11

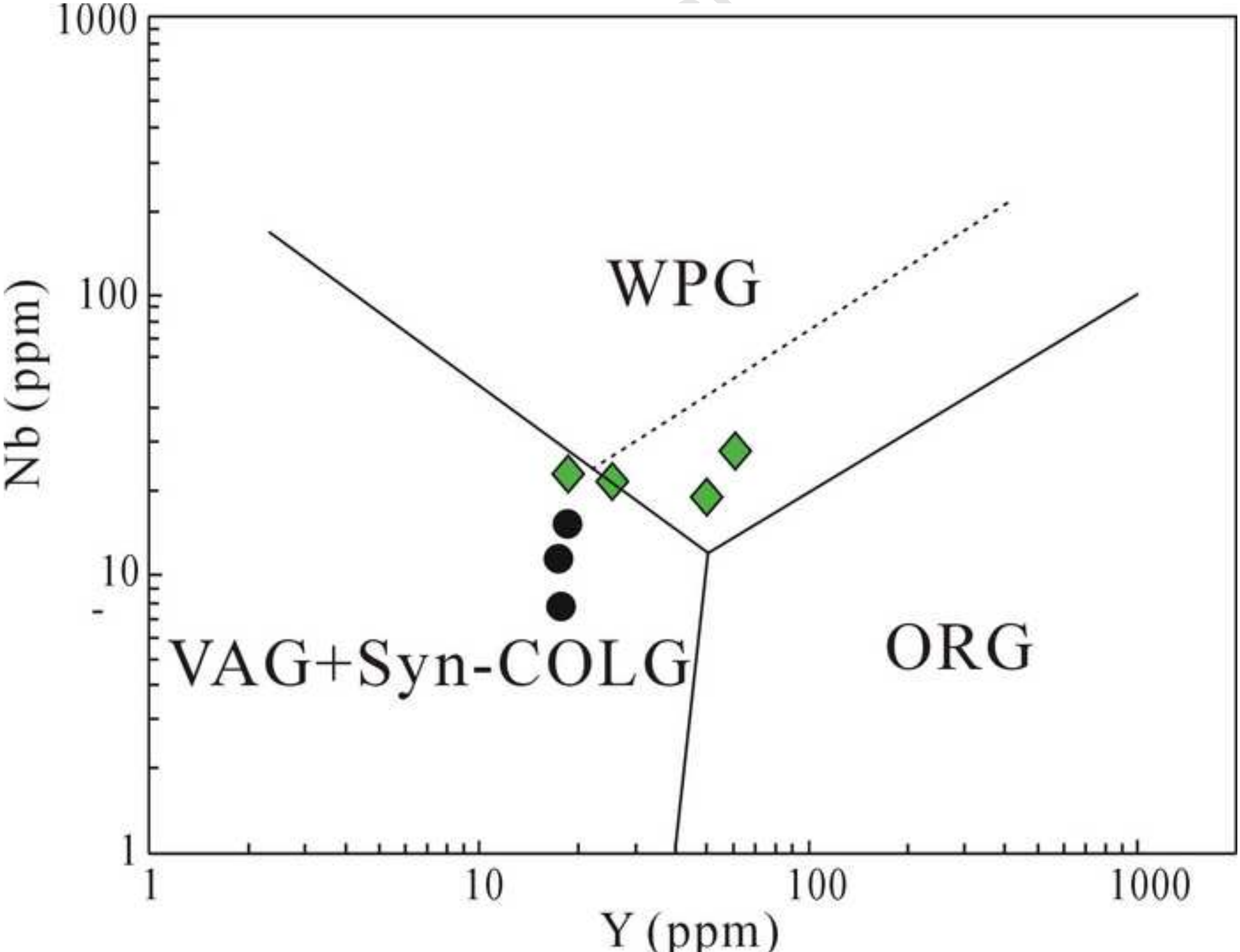

Figure 12

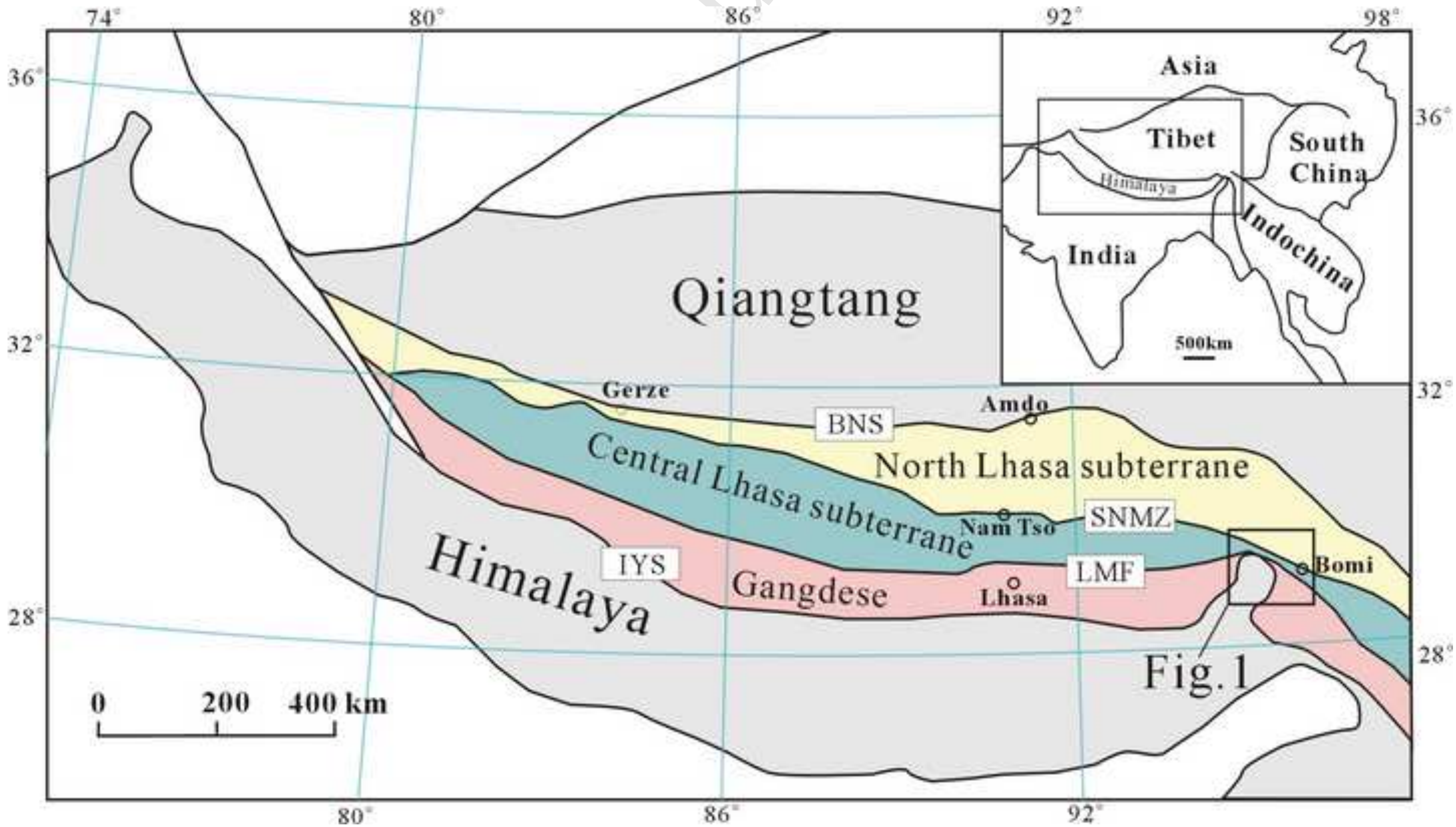
74°
80°
86°
92°
98°
36°
32°
28°
Asia
Tibet
South China
Himalaya
Indochina
India
500km
Qiangtang
Gerze
BNS
Amdo
North Lhasa subterrane
Central Lhasa subterrane
Nam Tso
SNMZ
IYS
LMF
Bomi
Himalaya
Gangdese
Lhasa
Fig.1
0
200
400 km